HHS Public Access

Author manuscript

Nature. Author manuscript; available in PMC 2017 June 06.

Published in final edited form as:

Nature. 2016 October 20; 538(7625): 383–387. doi:10.1038/nature19818.

Cortico-fugal output from visual cortex promotes plasticity of innate motor behaviour

Bao-hua Liu[1,2], **Andrew D. Huberman**[3], and **Massimo Scanziani**[1,2,4]

[1]Howard Hughes Medical Institute and Center for Neural Circuits and Behavior, University of California San Diego, La Jolla, California 92093-0634, USA

[2]Neurobiology Section and Department of Neuroscience, University of California San Diego, La Jolla, California 92093-0634, USA

[3]Department of Neurobiology, Stanford University School of Medicine, Palo Alto, California 94305, USA

[4]Department of Physiology, University of California San Francisco, San Francisco, California 94143-0444, USA

Abstract

The mammalian visual cortex massively innervates the brainstem, a phylogenetically older structure, via cortico-fugal axonal projections[1]. Many cortico-fugal projections target brainstem nuclei that mediate innate motor behaviours, but the function of these projections remains poorly understood[1–4]. A prime example of such behaviours is the optokinetic reflex (OKR), an innate eye movement mediated by the brainstem accessory optic system[3,5,6], that stabilizes images on the retina as the animal moves through the environment and is thus crucial for vision[5]. The OKR is plastic, allowing the amplitude of this reflex to be adaptively adjusted relative to other oculomotor reflexes and thereby ensuring image stability throughout life[7–11]. Although the plasticity of the OKR is thought to involve subcortical structures such as the cerebellum and vestibular nuclei[10–13], cortical lesions have suggested that the visual cortex might also be involved[9,14,15]. Here we show that projections from the mouse visual cortex to the accessory optic system promote the adaptive plasticity of the OKR. OKR potentiation, a compensatory plastic increase in the amplitude of the OKR in response to vestibular impairment[11,16–18], is diminished by silencing visual cortex. Furthermore, targeted ablation of a sparse population of cortico-fugal neurons that specifically project to the accessory optic system severely impairs OKR potentiation. Finally, OKR potentiation results from an enhanced drive exerted by the visual cortex onto the accessory optic system. Thus, cortico-fugal projections to the brainstem enable the visual cortex, an area that has been principally studied for its sensory processing function[19], to plastically adapt the execution of innate motor behaviours.

Author Contributions B.L. and M.S. designed the study. B.L. performed all experiments and data analysis. A.D.H. shared the Hoxd10-GFP mouse line. B.L. and M.S. wrote the manuscript.

Author Information The authors declare no competing financial interests. Readers are welcome to comment on the online version of the paper. Correspondence and requests for materials should be addressed to B.L. (lbaohua@ucsd.edu) or M.S. (massimo@ucsf.edu).

Online Content Methods, along with any additional Extended Data display Items and Source Data, are available in the online version of the paper; references unique to these sections appear only in the online paper.

Although the OKR is innate, it is also plastic[7–11]. Indeed, impairment of the vestibulo-ocular reflex, an innate oculomotor behaviour that works with the OKR to stabilize retinal images, leads to a compensatory increase in the amplitude of the OKR[11,16–18]. The compensatory increase in OKR relative to the vestibulo-ocular reflex is a striking example of how reflexes are plastically adjusted relative to each other to ensure appropriate motor behaviour. The adaptive plasticity of the OKR is classically studied by impairing the vestibulo-ocular reflex using lesions of the vestibular organ[11,14,16,17]. We used this experimental paradigm to determine whether the visual cortex is involved in the ensuing compensatory increase in OKR amplitude and to identify the underlying neural circuits.

We elicited a horizontal OKR (here referred to as OKR) in head-fixed adult mice by displaying on a virtual drum a vertical grating that drifted along the azimuth in an oscillatory manner; at the same time, we monitored the right eye with a camera (Fig. 1a, b and Extended Data Fig. 1a–d; Methods). We computed the gain of the OKR as the amplitude of the eye trajectory normalized to the amplitude of the grating trajectory (Methods; Extended Data Fig. 1). The OKR gain depended on the spatial and oscillation frequencies of the grating and varied from animal to animal[7,20] (Fig. 1c and Extended Data Fig. 1g).

A bilateral vestibular lesion (Methods) led to a robust compensatory increase in OKR gain (OKR potentiation). Mice recovered from the surgery in their home cages and the OKR was assessed before and two, four and six days after surgery (Fig. 1d, top). Two days after surgery, OKR gain was potentiated by more than 50% (53 ± 11% (mean ± s.e.m., $P = 4 \times 10^{-4}$; averaged over all oscillation frequencies), and this potentiation lasted for at least six days after surgery (day 4: 38 ± 8%, $P = 3$ a1 10^{-4}; day 6: 41 ± 9%, $P = 6 \times 10^{-4}$; Fig. 1d, e). On average, the potentiation was greater for higher oscillation frequencies (Fig. 1f). Thus, a vestibular lesion leads to strong OKR potentiation.

To investigate whether the visual cortex contributes to OKR potentiation, we silenced this area bilaterally by photostimulating cortical γ-aminobutyric acid (GABA)-releasing inhibitory neurons expressing the light-sensitive cation channel channelrhodopsin 2 (ChR2; Extended Data Fig. 2a; Methods). Before vestibular lesioning, cortical silencing (Extended Data Fig. 2b) led to only a small reduction in OKR gain (referred to as the cortical contribution to OKR gain; 10.9 ± 1.7%, $P = 4 \times 10^{-5}$; averaged over all frequencies; Fig. 1d, g and Extended Data Fig. 3a–c). Notably, in the same animals, cortical silencing two days after surgery led to a much stronger reduction in OKR gain (24.4 ± 1.8%, $P = 4 \times 10^{-5}$; Fig. 1d, g and Extended Data Fig. 3a–c). Thus the cortical contribution to OKR gain more than doubles after a bilateral vestibular lesion. To quantify the contribution of the visual cortex to OKR potentiation we used a potentiation index, PI (Methods; Extended Data Fig. 3c). PI is 1 if OKR potentiation is abolished upon cortical silencing and is 0 if the cortical contribution to OKR gain is unaffected by the vestibular lesion. The cortical contribution to OKR potentiation was between 0.1 and 1.16 and averaged 0.54 ± 0.10 across all oscillation frequencies (Fig. 1h and Extended Data Fig. 3d) indicating that at least half of OKR potentiation may depend on the visual cortex. In sham-lesioned animals (see Methods), OKR potentiation was absent and the cortical contribution to OKR gain was unaffected (Extended Data Fig. 3e, f). Thus, the contribution of the visual cortex to OKR gain increases

strongly after vestibular lesioning, indicating that the visual cortex has a prominent role in OKR potentiation.

Continuous OKR stimulation can also lead to OKR potentiation[7,10]. To determine whether this less invasive form of OKR potentiation also depends on the visual cortex, we exposed animals to continuous OKR stimulation for about 30 min. This protocol led to a progressive increase in OKR gain (50 ± 6%, $P = 4 \times 10^{-6}$; Extended Data Fig. 4a–c; Methods) and to an increase in the cortical contribution to OKR gain (from 5 ± 2% to 16 ± 2%, $P = 6 \times 10^{-4}$; Extended Data Fig. 4d), accounting for 33 ± 7% of OKR potentiation ($P = 5 \times 10^{-4}$; Extended Data Fig. 4c, e). Thus, the visual cortex contributes to OKR potentiation induced by vestibular lesioning or continuous OKR stimulation.

Through what pathway does the visual cortex influence OKR potentiation? Because the midbrain nuclei of the accessory optic system (AOS) represent the first stage downstream of the retina in the circuit that mediates the OKR[3,5,6], we investigated whether mouse visual cortex targets these structures. The horizontal OKR is mediated by the AOS structure composed of the apposed optic tract and dorsal-terminal nuclei (NOT-DTN)[3,5,6]. To identify the NOT-DTN, we used the Hoxd10-GFP mouse, in which retinal ganglion cells (RGCs) innervating the AOS express green fluorescent protein (GFP; Extended Data Fig. 5a). We verified the extent to which Hoxd10-GFP fluorescence delineated the NOT-DTN using c-Fos immunostaining (Methods). OKR stimulation for 60 min enhanced c-Fos expression in neurons located at coordinates corresponding to the NOT-DTN (Extended Data Fig. 5a–d). Furthermore, Hoxd10-GFP fluorescence overlapped with the enhanced expression of c-Fos in the NOT-DTN (overlap coefficient 86.4 ± 0.8%, $n = 43$ slices from 4 mice; Extended Data Fig. 5c). OKR stimulation did not enhance c-Fos expression in other visual nuclei not directly involved in OKR, such as the superior colliculus and ventral lateral geniculate nucleus (vLGN) (Extended Data Fig. 5e, f). Thus, we can unequivocally identify the NOT-DTN in mice. Stereotactic injections of retrograde fluorescent microspheres into the NOT-DTN (Methods) labelled layer 5 in the visual cortex (Fig. 2a) along with additional brain areas presynaptic to NOT-DTN (Extended Data Fig. 6a), indicating that the mouse visual cortex, like those of primates and carnivores[21,22], projects directly to NOT-DTN (Extended Data Fig. 6b).

To reveal the morphology of visual cortical neurons that projected to NOT-DTN, we injected the retrograde CAV2-Cre virus in the NOT-DTN of mice conditionally expressing tdTomato in the visual cortex (Methods). These injections revealed a sparse population of layer 5 pyramidal neurons (0.21% of layer 5 neurons) distributed across the primary and secondary visual cortices (Fig. 2b and Extended Data Fig. 6c). To verify that these cortico-fugal neurons form functional synaptic contacts with NOT-DTN neurons, we performed whole-cell recordings from NOT-DTN neurons in acute slices from mice expressing ChR2 in the visual cortex. Photo-stimulation of cortical axons triggered excitatory postsynaptic currents in NOT-DTN neurons (166 ± 258 pA, mean ± s.d.) with a short latency (3.9 ± 0.8 ms, mean ± s.d.) and little jitter (0.28 ± 0.21 ms, mean ± s.d.), mediated by both AMPA (α-amino-3-hydroxy-5-methyl-4-isoxazolepropionic acid) and NMDA (*N*-methyl-D-aspartate) receptors (Fig. 2c and Extended Data Fig. 6d). The monosynaptic identity of this projection was validated using subcellular ChR2-assisted circuit mapping (sCRACM; Extended Data Fig.

6e). Finally, to determine whether this cortico-fugal projection could drive NOT-DTN neurons, we recorded extracellularly from the NOT-DTN in anaesthetized mice (Methods). Optogenetic activation of the visual cortex increased the firing of NOT-DTN neurons with a short latency (5 ± 19.7 ms, median ± s.d.; Fig. 2d). Thus, cortico-fugal projections from mouse visual cortex to the NOT-DTN form functional excitatory synapses that can drive the activity of NOT-DTN neurons.

To determine whether cortico-fugal projections to the NOT-DTN are necessary for the cortical component of OKR potentiation, we selectively ablated NOT-DTN-projecting cortical neurons with diphtheria toxin. We infected the NOT-DTN with the retrograde CAV2-Cre virus in mice whose visual cortex had been injected with an AAV virus expressing the diphtheria toxin receptor (DTR) in a Cre-dependent manner (Methods; Fig. 3a). DTR-expressing neurons in the visual cortex were completely ablated 11 days after intraperitoneal diphtheria toxin injection (Fig. 3b). We tested the OKR and its modulation by visual cortex in the same mice at three time points: before diphtheria toxin injection, after diphtheria toxin injection and after vestibular lesioning (Fig. 3a, c). Before diphtheria toxin injection, cortical silencing reduced OKR gain by 14 ± 2% (P=4 × 10^{-7}; Fig. 3d), similar to control mice (Fig. 1g). By contrast, 11–12 days after diphtheria toxin injection, cortical silencing reduced OKR gain significantly less than before injection (7 ± 2%, P = 0.007; Fig. 3d), demonstrating that NOT-DTN-projecting cortical neurons modulate OKR gain. Crucially, two days after vestibular lesioning, OKR potentiation was significantly reduced in animals with an ablated cortico-NOT-DTN projection (1.25 ± 0.10; Fig. 3e) as compared to animals with an intact projection (that is, in animals injected with AAV-DTR and CAV-Cre but not diphtheria toxin (1.46 ± 0.13; n = 6)) or in control animals (1.51 ± 0.08; Fig. 3e). Furthermore, the residual OKR potentiation was nearly independent of visual cortex because cortical silencing led to a very small reduction in OKR gain (8 ± 2%; Fig. 3d and Extended Data Fig. 7), similar to the reduction observed in the same animals after diphtheria toxin injection but before vestibular lesioning. In these animals, the cortical contribution to OKR potentiation was only −0.02 ± 0.13, significantly smaller than in control animals (0.49 ± 0.11; P = 0.003). Thus, despite its sparseness, the population of visual cortico-fugal neurons projecting to the NOT-DTN is necessary for a large fraction of OKR potentiation and is entirely responsible for the cortical contribution to this phenomenon.

Because the cortical component of OKR potentiation relies on cortico-fugal projections to the NOT-DTN, we tested whether vestibular lesioning enhanced the ability of these projections to drive NOT-DTN activity. We targeted the NOT-DTN with extracellular linear probes as above (Fig. 4a). Isolated NOT-DTN units showed a preference for temporonasally moving visual stimuli presented to the contralateral eye, consistent with recordings in other mammals[23,24] (Fig. 4b and Extended Data Fig. 8a–e). Furthermore, local application of the $GABA_A$-receptor agonist muscimol suppressed NOT-DTN activity (57 ± 7%) and eliminated the OKR (90 ± 2%), consistent with the necessity of this structure to trigger the reflex[25] (Fig. 4c and Extended Data Fig. 8f). Optogenetic silencing of visual cortex led to a stronger reduction in NOT-DTN activity in mice that had undergone vestibular lesioning than in naive mice (21.1 ± 2.3% versus 12.7 ± 1.5%, P = 0.003; Fig. 4d, e). Furthermore, the reduction in NOT-DTN activity correlated well with the simultaneously observed reduction

in OKR gain (correlation coefficient 0.55, $P = 0.0007$; Fig. 4f). Thus, after a vestibular lesion, NOT-DTN activity depends more on visual cortex than in naive animals.

Can the cortical contribution to OKR potentiation be accounted for by the influence of the cortex on NOT-DTN activity? NOT-DTN-projecting cortical neurons could also contribute to OKR potentiation through collateral projections to targets downstream from the NOT-DTN. We addressed this question functionally and anatomically. We first established the 'transfer function'—the relationship between OKR gain and NOT-DTN activity (Fig. 5a). If the cortical contribution to OKR potentiation is mediated through its impact on NOT-DTN activity, reducing NOT-DTN activity through cortical silencing will lead to a reduction in OKR gain predicted by the transfer function (Fig. 5a, left). If, alternatively, visual cortex also mediates OKR potentiation through projections downstream from the NOT-DTN, cortical silencing will lead to a decrease in OKR gain not predicted by the transfer function (Fig. 5a, right). We recorded NOT-DTN activity while monitoring the OKR in response to stimuli of various spatial frequencies that elicit a wide range of OKR velocities (Extended Data Fig. 9a). The dependence of NOT-DTN activity on the spatial frequency of stimuli was similar to that of the OKR gain (Extended Data Fig. 9b, c and Fig. 1c; this was not the case for other visual nuclei, Extended Data Fig. 9e, f). We fitted the transfer function $G = kR^x$ to the data points relating NOT-DTN activity (R) to OKR gain (G; x, exponent; k, proportionality factor) (Fig. 5b and Extended Data Fig. 9d). In both naive and lesioned animals, the reduction in OKR gain that resulted from cortical silencing was accurately predicted by the concomitant reduction in NOT-DTN activity ($P = 0.71$ for naive, 0.84 for lesion, Kolmogorov-Smirnov test; Fig. 5c–e). Cortical silencing simply shifted the data points along the transfer function obtained without cortical silencing, bringing them closer to the origin. This shift was much larger in lesioned than in naive animals (0.19 ± 0.01 versus 0.09 ± 0.01, lesioned versus naive; $P = 7 \times 10^{-10}$; quantified as vector length, see Methods; Extended Data Fig. 9g–j). Thus, the cortical contribution to OKR potentiation can be fully accounted for by its increased impact on NOT-DTN activity. Finally, we determined whether NOT-DTN-projecting cortical neurons send collaterals to additional subcortical structures. Consistent with the above functional results, we did not observe collaterals of NOT-DTN-projecting cortical neurons in downstream structures involved in OKR (the pontine nuclei[26], pre-oculomotor nuclei near the periaqueductal grey, inferior olive or cerebellum; Fig. 5f and Extended Data Fig. 10). Instead, we observed labelled axons in the vLGN, superior colliculus and striatum. As the vLGN and superior colliculus project to the NOT-DTN[3,27] (Extended Data Fig. 6a), they could also contribute to the increased drive of the NOT-DTN. However, OKR stimulation evoked only weak activity in the superior colliculus or vLGN (multiunit activity, 2.2 ± 0.4 spikes per s for superior colliculus and 1.2 ± 0.3 spikes per s for vLGN) and this activity did not correlate with OKR gain (Extended Data Fig. 9e, f). These two structures are thus unlikely to contribute substantially to the cortical component of OKR potentiation (see also Extended Data Fig. 5e, f).

These results show that the visual cortex has an essential role in OKR potentiation and identify the cortico-fugal projection to the NOT-DTN as the anatomical and physiological substrate that underlies OKR potentiation.

The cortex-independent fraction of OKR potentiation may be mediated by subcortical structures such as the cerebellum and vestibular nuclei, consistent with their established roles in OKR plasticity[10–13]. Thus, cortico-fugal projections from the visual cortex to the brainstem may work with these subcortical structures to mediate the compensatory potentiation of the reflex.

Cortico-fugal projections from sensory areas to brainstem nuclei can modulate innate behaviours[28,29] and learning-dependent plasticity[30], but our understanding of the functions of those projections is still very limited. In primates and carnivores, the visual cortex contributes to some properties of the OKR, including directional symmetry of the reflex and gain[5]. The demonstration that cortico-fugal projections to the AOS play an essential role in the plastic adaptation of the OKR expands our understanding of how the innervation of phylogenetically older structures by the mammalian cortex can improve the performance of reflexive behaviour in an experience-dependent manner. Thus, the visual cortex must be regarded not only as an area for sensory processing but as an area that, through its output to the brainstem, is directly involved in the plasticity of fundamental innate motor behaviours.

METHODS

Mice

Experiments were performed in accordance with the regulations of the Institutional Animal Care and Use Committee of the University of California, San Diego.

We used the following mouse lines: VGAT-ChR2-EYFP[31] (Jackson Labs #014548), PV-Cre[32] (Jackson Labs #008069), Gad2-Cre[33] (Jackson Labs #010802) and Hoxd10-GFP[34] (MMRRC #032065-UCD). Mice were bred by crossing homozygous VGAT-ChR2-EYFP, PV-Cre or Gad2-Cre males (all lines with a C57BL/6 background) with wild-type ICR females or homozygous Hoxd10-GFP females (ICR background) to C57BL/6 males. Mice were housed in a vivarium with a reversed light cycle (12 h day-12 h night). Mice of both genders were used for experiments at postnatal ages of 2–6 months.

Viral and retrobead injections

We used the following adeno-associated viruses (AAV) and canine adenovirus (CAV2):

For the Cre recombinase (Cre)-dependent expression of Channelrhodopsin2 (ChR2)[35,36]: AAV2/9.CAGGS.Flex.ChR2.tdTomato.SV40 (Addgene 18917; UPenn Vector Core).

For the Cre-dependent expression of tdTomato: AAV2/1.CAG.Flex.tdTomato. WPRE.bGH (Allen Institute 864; UPenn Vector Core).

For the expression of Cre: AAV2/9.hSyn.HI.eGFP-Cre.WPRE.SV40 (UPenn Vector Core).

For Cre-dependent expression of the diphtheria toxin receptor (DTR)[37]: AAV2/1.Flex.DTR.GFP (Jessell laboratory; produced at UNC Vector Core).

For retrograde expression of Cre: CAV2.Cre[38] (Montpellier vector platform).

Optogenetic silencing of visual cortex

AAV 2/9.CAGGS.Flex.ChR2.tdTomato. SV40 was bilaterally injected into the visual cortex of newborn PV-Cre or Gad2–Cre pups (postnatal day (P) 0–2). The virus was loaded into a bevelled glass micropipette (tip diameter 20–40 μm) mounted on a Nanoject II (Drummond) attached to a micromanipulator. Pups were anaesthetized by hypothermia and secured in a molded platform. In each hemisphere the virus was injected at two sites along the medial-lateral axis of the visual cortex. At each site we made three bolus injections of 28 nl. Each were at three different depths between 300 and 600 μm. Protein expression was verified by epi-fluorescent illumination through a dissection microscope (Leica MZ10F). Experiments were performed on animals with expression over the entire extent of visual cortex.

Optogenetic stimulation of visual cortex *in vivo* or cortico-fugal axons *in vitro*

AAV2/9.hSyn.HI.EGFP-Cre.WPRE.SV40 and AAV2/9.CAGGS.Flex.ChR2.tdTomato were mixed in 1:20 ratio. The mixture was injected into the visual cortex of newborn C57BL/6 pups (as described above). Protein expression was verified by epi-fluorescent illumination.

Retrogradely labelling of NOT-DTN-projecting neurons in the visual cortex

Adult Hoxd10-GFP mice were anaesthetized with ~2% isoflurane (vol/vol) in O_2. The depth of anaesthesia was monitored with the toe-pinch response. The eyes were protected from drying by artificial tears. We cut open the scalp and thinned the skull to create a window of ~300–500 μm diameter. The remaining layer of bone in the window was thin enough to allow the penetration of the beveled glass pipette. A bolus of retrograde fluorescent microspheres (RetroBeads, Lumafluor Inc.) or CAV2.Cre virus (40 nl RetroBeads or 20 nl CAV2 virus) was injected into the NOT-DTN (coordinates (anteroposterior axis (AP) relative to bregma; mediolateral axis (ML) relative to the midline): AP: −1,260 μm; ML: 3,080 μm; depth: 1,960 μm; coordinates were adjusted based on the distance between bregma and lambda on mouse skull) using an UltraMicroPump (UMP3, WPI). The wound was sutured with a few stitches of 6–0 suture silk (Fisher Scientific NC9134710). Mice were perfused 3 days after the retrobead injection or 2 weeks after the CAV2 injection.

Ablation of the cortico-fugal projection to the NOT-DTN

AAV2/1.Flex.DTR. GFP was bilaterally injected into the visual cortex of VGAT-ChR2-EYFP pups between P0 and P2. CAV2.Cre virus was subsequently stereotactically injected into the NOT-DTN (same coordinates as above) bilaterally in mice of 2–6 months of age. Three to four weeks later we injected diphtheria toxin (DT 40 ng/g) intraperitoneally three times on alternate days. The OKR was assessed 11 or 12 days after the first diphtheria toxin injection. In control experiments, diphtheria toxin was replaced with PBS or diphtheria toxin was injected into mice that had not been infected with AAV2/1.Flex.DTR.GFP.

Head bar implantation and cranial window

Mice were implanted with a T-shaped head bar for head fixation. Mice were anaesthetized using ~2% isoflurane. The scalp and fascia were removed and a metal head bar was mounted over the midline using dental cement (Ortho-Jet powder; Lang Dental) mixed with black paint (iron oxide).

We created a cranial window of ~3 × 3 mm (1.5–4.5 mm lateral to midline and 2.3–5.2 mm posterior to bregma) over the visual cortex on each hemisphere by gently thinning the skull until it appeared transparent when wetted by saline solution. The window was then covered with a thin layer of crazy glue. Following the surgery animals were injected subcutaneously with 0.1 mg/kg buprenorphine and allowed to recover in their home cage for at least 1 week. Several days before the test, mice were familiarized with head fixation in the recording setup. No visual stimulation was given.

Assessment of the OKR

Visual stimulation—The horizontal OKR was elicited by a 'virtual drum' system[39]. Three computer LED monitors (Viewsonic VX2450wm-LED, 60-Hz refresh rate, gamma-corrected) were mounted orthogonally to each other to form a square enclosure that covered ~270° of visual field along the azimuth. The mouse head was immobilized at the centre of the enclosure with the nasal and temporal corners of the eye leveled. Visual stimuli were generated with Psychophysics Toolbox 3 running in Matlab (Mathworks). To ensure synchronized updating across multiple monitors we used AMD Eyefinity Technology (ATI FirePro V4800). The monitors displayed a vertical sinusoidal grating whose period (spacing between stripes) was adjusted throughout the azimuthal plane such that the projection of the grating on the eye had constant spatial frequency. In other words, the spatial frequency of the grating was perceived as constant throughout the visual field, as if the grating was drifting along the surface of a virtual drum. The dependence of pixel brightness on monitor coordinates was obtained by using this equation: $B = L + L \times C \times \sin(2\pi \times x_{deg} \times SF)$, where B is the brightness of pixels, L is the luminance in cd/m^2, C is the contrast, SF is the spatial frequency and x_{deg} is the azimuth of pixels in degrees, which is transformed from the Cartesian coordinates of the monitor into the cylindrical coordinates of the virtual drum by the following formula: $x_{deg} = \tan^{-1}(x_{pix}/D)$, where x_{pix} is the horizontal pixel position in Cartesian coordinates and D is the distance from the centre of the monitors to the eye (Extended Data Fig. 1a).

The grating drifted clockwise or counterclockwise in an oscillatory manner[7,11] (oscillation amplitude ± 5°; grating spatial frequency: 0.04–0.45 cpd; oscillation frequency 0.2–1 Hz, corresponding to a peak velocity of the stimulus of 6.28–31.4° s^{-1}; contrast: 80%; mean luminance: 40 cd/m^2). We chose the duration of the visual stimulus to allow the presentation of an integral number of oscillatory cycles (10 or 15 s for OKR test only; 7.5 s for simultaneous NOT-DTN electrophysiology and OKR test). Trials were spaced by an inter-stimulation interval of at least 8 s. The inter-stimulation interval following trials of cortical silencing was increased to 20 s. To measure the oscillation frequency tuning, spatial frequency was kept constant at 0.08 cpd; to measure the spatial frequency tuning oscillation, the frequency was kept at 0.4 Hz.

To obtain the transfer function, we varied the spatial frequency of the visual stimulus rather than the oscillation frequency because OKR peak velocity is strongly modulated by spatial frequency and much less so by the oscillation frequency (consistent with previous observations[7,40]; Extended Data Fig. 9a). The spatial frequency was varied from 0.04 to 0.45 cpd, and the oscillation frequency was kept constant at 0.4 Hz.

To evaluate the directional preference of NOT-DTN neurons, one monitor was positioned 20 cm from the eye contralateral to the side of recording. Full-field sinusoidal drifting gratings (oscillation frequency: 1 Hz; spatial frequency: 0.08 cpd; mean luminance: 50 cd/m^2; contrast: 100%) were used. Gratings were randomly presented at 12 equally spaced positions. The duration of the visual stimulus was 2 s and the inter-trial interval was 2.2 s.

To visualize NOT-DTN with c-Fos immunostaining (c-Fos is an immediate early gene expressed in response to neuronal activity), OKR was elicited by drum stimulation of various spatial frequencies (0.04–0.45 cpd) with oscillation frequency 0.4 Hz, contrast 100% and luminance 50 cd/m^2. Trials of oscillatory motion lasted for 15 s and were followed by an inter-trial interval of 8 s. The whole stimulation procedure took 60 min.

Monitoring eye movements by infrared video-oculography[41,42]—The movement of the right eye was monitored through a high speed infrared (IR) camera (Imperx IPX-VGA 210; 100 Hz). The camera captured the reflection of the eye on an IR mirror (transparent to visible light, Edmund Optics #64–471) under the control of custom labview software and a frame grabber (National Instrument PCIe-1427). The pupil was identified online by thresholding pixel values or *post hoc* by combining thresholding and morphology operation and its profile was fitted with an ellipse to determine the centre. The eye position was measured by computing the distance between the pupil centre and the corneal reflection of a reference IR LED placed along the optical axis of the camera. To calibrate the measurement of the eye position, the camera and the reference IR LED were moved along a circumference centred on the image of the eye by ± 10° (Extended Data Fig. 1b).

Optogenetic silencing[43] or stimulation of the visual cortex

Three mouse lines (VGAT-ChR2-EYFP, PV-Cre and Gad2-Cre) were used in experiments involving optogenetic silencing of the visual cortex. They are equally efficient in silencing activity of visual cortex and interchangeable. VGAT-ChR2-EYFP mice were used in most of the silencing experiments, except in experiments illustrated in Extended Data Fig. 2a (PV-Cre line) and Extended Data Fig. 3b (all 3 lines). To photostimulate ChR2-expressing cortical inhibitory neurons *in vivo*, a 470-nm blue fibre-coupled LED (1 mm diameter, Doric Lenses) was placed ~5–10mm above the cranial windows of each hemisphere. We restricted the illumination to the tissue under the cranial window by covering neighbouring areas with dental cement. An opaque shield of black clay prevented LED light from directly reaching the eyes. The total light power out of the LED fibre was 15–20 mW. Trials were alternated between visual stimulus alone and visual stimulus plus LED. The LED was turned on during the whole period of visual stimulation and turned off by ramping down the power over 0.5 s to limit rebound activation of the visual cortex.

To photostimulate cortical input to the NOT-DTN *in vivo*, blue light illuminated only the visual cortex ipsilateral to the NOT-DTN where the probe was inserted. **Vestibular lesions**. We dissected out the tissue overlying the horizontal semicircular canal in mice under ~2% isoflurane anaesthesia. A small hole was drilled in the canal with a miniature Busch Bur (0.25 mm, Gesswein) and the endolymph was partially drained. The horizontal semicircular canal was plugged with bone wax (FST 19009–00) to seal the opening and reduce the flow

of the endolymph within the canal. The wound was sutured with a few stitches of 6/0 suture. Mice recovered for two days in their home cages before being tested for OKR. Sham lesions were done in the same way except that no hole was drilled and no wax was introduced in the semicircular canal.

Continuous OKR stimulation

OKR gain (spatial frequency: 0.1 cpd; oscillation frequency: 0.4 Hz; contrast: 100%; mean luminance: 35 cd/m^2) was assessed 1 day before and 1 h before OKR training. Two sessions (12 min) were used to minimize the effect of visual stimulation during OKR evaluation on OKR gain. During continuous OKR stimulation, a drum of the same visual parameters ran continuously for 38 min. OKR gain was then assessed again 12 min after OKR stimulation was finished.

In vivo recordings from the NOT-DTN, superior colliculus or vLGN of awake or anaesthetized mice

Mice were implanted with a T-shaped head bar for head fixation in the same way as described above for the OKR assessment, except that the procedure was done stereotactically with the help of an inclinometer (Digi-Key electronics 551-1002-1-ND). The inclinometer allowed us to calibrate the inclination of the two axis of the T bar relative to the anteroposterior (AP) and mediolateral (ML) axes of the skull before fixing it to the skull with dental cement. Three reference points with known coordinates were marked on the mouse skull because both bregma and lambda were inevitably masked by the dental cement holding the head bar. The head post on the recording rig was also calibrated with the same inclinometer to ensure that the recording probes were in register with the skull.

Recordings from awake animals were performed using a method similar to that described previously[43]. One to two weeks before recording, mice were familiarized with head fixation within the recording setup over the course of two to four 50-min sessions. One day before recording, mice were anaesthetized with ~2% isoflurane. Whiskers and eyelashes contralateral to the recording side were trimmed to prevent interference with infrared video-oculography. To access the NOT-DTN we made an elongated, anteroposteriorly oriented craniotomy (~0.4 × 0.8 mm) around the coordinates of −3 mm (anteroposterior) and 1.3 mm (mediolateral). The coordinates were adjusted based on the distance between bregma and lambda on mouse skull. The craniotomy was then covered by Kwik-Cast Sealant (WPI).

On the day of recording, after peeling off the Kwik-Cast cover, a drop of artificial cerebrospinal fluid (ACSF; in mM, 140 NaCl, 2.5 KCl, 2.5 $CaCl_2$, 1.3 $MgSO_4$, 1.0 NaH_2PO_4, 20 HEPES and 11 glucose, pH 7.4) was placed in the well of the craniotomy to keep the exposed brain moist. A 16-channel linear silicon probe (NeuroNexus a1x16-5mm-25-177) mounted on a manipulator (Luigs &Neumann) was slowly advanced into the brain to a depth of 2,000–2,200 μm. The occurrence of direction modulated activity upon visual stimulation was used to identify the NOT-DTN (see data analysis below). The probe was stained by lipophilic DiI to label the recording track for *post hoc* verification of successful targeting of the NOT-DTN.

Recordings were not started until 20 min after insertion of the probe into the NOT-DTN. Signals were amplified 400-fold, band-pass filtered (0.3–5,000 Hz, with the presence of a notch filter) with an extracellular amplifier (A-M Systems 3600) and digitized at 32 kHz (National Instrument PCIe-6259) with custom-written software in Matlab. Raw data were stored on a computer hard drive for offline analysis. At the end of the recording session, brains were fixed by transcardial perfusion of 4% paraformaldehyde for histological analysis.

Recordings from the superior colliculus or vLGN were done in the same way except that the coordinates of the craniotomy were 3.5 mm (anteroposterior) and 1 mm (mediolateral) for the superior colliculus and 2.5 mm (anteroposterior) and 2.3 mm (mediolateral) for the vLGN.

For recordings from anaesthetized mice we used the same procedures as described above except that (1) the familiarization step was omitted and the craniotomy was performed immediately before recording; (2) animals were anaesthetized with urethane (1.2 g/kg, intraperitoneal) and given the sedative chlorprothixene (0.05 ml of 4 mg/ml, intramuscular), as previously described[44]; (3) body temperature was maintained at 37 °C using a feedback-controlled heating pad (FHC 40-90-8D); (4) a uniform layer of silicone oil was applied to the eyes to prevent drying; and (5) lactated Ringer's solution was administrated at 3 ml/kg/h to prevent dehydration.

In vitro recordings

Mice at postnatal days 15–30 were anaesthetized by intraperitoneal injection of ketamine and xylazine (100 mg/kg and 10 mg/kg, respectively), perfused transcardially with cold (0–4 °C) slice cutting solution ((in mM) 80 NaCl, 2.5 KCl, 1.3 NaH_2PO_4, 26 $NaHCO_3$, 20 D-glucose, 75 sucrose, 0.5 sodium ascorbate, 4 $MgCl_2$ and 0.5 $CaCl_2$, 315 mOsm, pH 7.4, saturated with 95% O2/5% CO_2) and decapitated. Brains were sectioned into coronal slices of 300–400 μm in cold cutting solution with a Super Microslicer Zero1 (D.S.K.). Slices containing the NOT-DTN were incubated in a submerged chamber at 34 °C for 30 min and then at room temperature (~21 °C) until used for recordings. During the whole procedure, the cutting solution was bubbled with 95% O_2/5% CO_2.

Whole-cell recordings were done in ACSF (in mM: 119 NaCl, 2.5 KCl, 1.3 NaH_2PO_4, 26 $NaHCO_3$, 20 D-glucose, 0.5 sodium ascorbate, 4 $MgCl_2$, 2.5 $CaCl_2$, 300 mOsm, pH 7.4, saturated with 95% O_2/5% CO_2). The ACSF was warmed to ~30 °C and perfused at 3 ml/min. NOT-DTN neurons were visualized with DIC infrared video-microscopy under a water immersion objective (40×, 0.8 NA) on an upright microscope (Olympus BX51WI) with an IR CCD camera (Till Photonics VX44). Whole-cell voltage-clamp recordings were performed with patch pipettes (borosilicate glass; Sutter Instruments) using a caesium-based internal solution ((in mM) 115 $CsMeSO_4$, 1.5 $MgCl_2$, 10 HEPES, 0.3 Na_3GTP, 4 MgATP, 10 Na_2-phosphocreatine, 1 EGTA, 2 QX-314-Cl, 10 BAPTA-tetracesium, 0.5% biocytin, 295 mOsm, pH 7.35). AMPA receptor-mediated EPSCs were recorded at the reversal potential for IPSCs (~−65 mV) and NMDA receptor-mediated EPSCs were recorded at +40 mV in the presence of the $GABA_A$ receptor antagonist gabazine (5 μM, Tocris 1262) and the AMPA receptor antagonist NBQX (10 μM, Tocris 1044). To verify monosynaptic

connectivity, we isolated NMDA receptor-mediated EPSCs in the presence of NBQX and high Mg^{2+} concentration (4 mM) or monosynaptic AMPA receptor-mediated EPSCs by a modified sCRACM approach[45] in the presence of tetrodotoxin (TTX; 1 μM, Tocris 1069), 4-aminopyridine (4-AP; 1.5 mM, Abcam ab120122) and tetraethylammonium (TEA; 1.5 mM, ab120275). EPSCs were acquired and filtered at 4 kHz with a Multiclamp 700B amplifier, and digitized with a Digidata 1440A at 10 kHz under the control of Clampex 10.2 (Molecular Devices). Data were analysed offline with Clampfit 10.2 (Molecular Device). To photostimulate ChR2-expressing cortico-fugal axons, we delivered blue light using a collimated LED (470 nm) and a T-Cube LED Driver (Thorlabs) through the fluorescence illuminator port and the 40 × objective. Light pulses of 10 ms and 5.5 mW/mm^2 were given with a 20 s inter-stimulus interval. After recordings, slices were fixed by 4% paraformaldehyde for histology.

Pharmacological silencing of the NOT-DTN

After implanting the head bar, under anaesthesia (2% isoflurane), we dissected out part of the skull and removed, by aspiration, the area of the cortex and hippocampus overlaying the NOT-DTN. The identity of the NOT-DTN was assessed visually by its anatomy and stereotactic coordinates and verified electrophysiologically (see data analysis below). After the surgery, the mice were head-fixed and isoflurane was withdrawn. For at least the next 45 min, OKR performance and NOT-DTN activity were recorded. The $GABA_A$ receptor agonist muscimol (0.2–1 mM in ACSF) was applied on top of the NOT-DTN. It took ~30 min for muscimol to silence the NOT-DTN, as assessed electrophysiologically. Pupillary dilation, as a side effect of silencing the olivary pretectal nucleus, was counteracted by topical application of 2% pilocarpine hydrochloride (agonist of muscarinic receptor, Tocris 0694) in saline to both eyes.

Histochemistry

Mice were perfused transcardially first with phosphate buffered saline (PBS, pH 7.4) and then with 4% paraformaldehyde in PBS (pH 7.4) under anaesthesia (ketamine 100 mg/kg and xylazine10 mg/kg; intraperitoneal injection). Brains were removed from the skull, post-fixed overnight in 4% paraformaldehyde and then immersed in 30% sucrose in PBS until they sank. Brains were subsequently coronally sectioned (40–60 μm sections) with a sliding microtome (Thermo Scientific HM450). Slices were incubated in blocking buffer (PBS, 5% goat serum (Life Technologies 16210-072), 1% Triton X-100) at room temperature for 2 h and then incubated with primary antibodies in blocking buffer at 4 °C overnight. The following primary antibodies were used: rabbit anti-GFP (1:1,000, Life Technologies A6455) and rabbit anti-c-Fos (1:1,000, Santa Cruz Biotechnology sc-52). The slices were washed three times with blocking buffer for 30 min each and then incubated with secondary antibodies conjugated with Alexa Fluor 488, 594 or 633 (1:800, Life Technologies A11008, A11012 or A21070, respectively) in blocking buffer for 2 h at room temperature. After being washed three times with blocking buffer for 10 min each, slices were mounted in Vectashield mounting medium containing DAPI (Vector Laboratories H1500).

For c-Fos immunostaining, 90 min after the beginning of OKR stimulation (30 min after 60-min OKR simulation was finished), animals were perfused transcardially first with PBS and

then with 4% paraformaldehyde in PBS. Brains were coronally sectioned into slices of 40 μm.

To reveal the morphology of NOT-DTN neurons filled with biocytin, following fixation and blocking (see above), we incubated the slices with streptavidin conjugated with Alexa Fluor 647 (1:500, Life Technologies s32357) in blocking buffer overnight and then washed the slices three times.

Images were acquired on a Leica SP5 confocal microscope, a Zeiss Axio Imager A1 epifluorescence microscope or an Olympus MVX10 stereoscope, and processed using ImageJ (National Institutes of Health).

Data analysis

Analysis of eye tracking and *in vivo* electrophysiology was performed using custom-written codes in Matlab. Analysis of *in vitro* electrophysiology was done with Clampfit 10.2 (Molecular Devices).

OKR gain

Saccade-like fast eye movements were removed from the recorded eye trajectory before computing OKR amplitude (Extended Data Fig. 1c). Saccades were detected as 'spikes' in the temporal derivative of the eye position (velocity) and replaced by linear interpolation. To derive the amplitude of the OKR we used the Fourier transform of the eye position as a function of time. The eye trajectories illustrated in this study are the averages of several cycles. The gain of the OKR was expressed as OKR gain = Amp_{eye}/Amp_{drum}, where Amp_{eye} is the amplitude of eye movement and Amp_{drum} the amplitude of drum movement. The OKR gain derived in the space domain is similar to that derived in the velocity domain (Extended Data Fig. 1f). In this study, we computed the gain in the space domain because deriving eye velocity from eye position introduces noise. Therefore, the OKR gain is 1 if the eye perfectly tracks the trajectory of the virtual drum and 0 if it does not track.

Cortical contribution to OKR gain

The cortical contribution to the OKR gain is expressed as the percentage reduction in OKR gain caused by cortical silencing and calculated as $\Delta V(\%) = (V_{control} - V_{silencing})/V_{control}$, where $V_{control}$ and $V_{silencing}$ are the values of the OKR gain measured under control conditions or during optogenetic cortical silencing, respectively.

OKR potentiation following vestibular lesion

OKR potentiation is calculated as $V_{post\ VL}/V_{pre\ VL}$, where $V_{pre\ VL}$ *and* $V_{post\ VL}$ are the values of the OKR gain measured before and after vestibular lesion, respectively.

Cortical contribution to OKR potentiation

The cortical contribution to OKR potentiation is expressed as $PI = (\Delta V_{post\ VL} - \Delta V_{pre\ VL})/(\Delta V_{max} - \Delta V_{pre\ VL})$, where $\Delta V_{pre\ VL}$ and $\Delta V_{post\ VL}$ are the cortical contribution to the OKR gain before and after vestibular lesioning, respectively, and ΔV_{max} is the maximum possible cortical contribution to the OKR gain assuming that the entire amount of OKR potentiation

depends on visual cortex. $\Delta V_{max} = (V_{post\ VL,\ control} - V_{pre\ VL,\ silencing})/V_{post\ VL,\ control}$. Hence PI is 1 if the entire amount of OKR potentiation depends on visual cortex and is 0 if the cortical contribution to OKR gain before vestibular lesion is the same as the cortical contribution to OKR gain after vestibular lesion ($\Delta V_{pre\ VL} = \Delta V_{post\ VL}$) (Extended Data Fig. 3c, d).

Cortical contribution to NOT-DTN activity

The cortical contribution to NOT-DTN activity is expressed as the cortical contribution to OKR gain but $V_{control}$ and $V_{silencing}$ are the firing rates of NOT-DTN neurons under control conditions or during optogenetic cortical silencing, respectively.

Unit isolation

Single units were isolated using spike-sorting Matlab codes, as described previously[43]. The raw extracellular signal was band-pass filtered between 0.5 and 10 kHz. Spiking events were detected with a threshold at 3.5 or 4 times the standard deviation of the filtered signal. Spike waveforms of four adjacent electrode sites were clustered using a *k*-means algorithm. After initial automated clustering, clusters were manually merged or split with a graphical user interface in Matlab. Unit isolation quality was assessed by considering refractory period violations and Fisher linear discriminant analysis. All units were assigned a depth according to the electrode sites at which their amplitudes were largest. Multi-unit spiking activity was defined as all spiking events exceeding the detection threshold after the removal of electrical noise or movement artefacts by the sorting algorithm. Individual spiking events were also assigned to one of the 16 recording sites according to where they showed the largest amplitude. For both single-unit activity and multi-unit activity, the visual response was computed as the mean firing rate during visual stimulation without baseline subtraction.

Units recorded from visual cortex were assigned as regular-spiking neurons or fast-spiking putative inhibitory neurons based on the trough-to-peak times of spike waveforms[43]. A threshold of 0.4 ms was used to distinguish fast-spiking from regular-spiking units.

Direction selectivity index

The boundary of the NOT-DTN was determined by the appearance of a temporonasal directional bias in the multi-unit response to the visual stimulus.

The preferred direction of an isolated NOT-DTN unit was determined by summing response vectors of 12 evenly spaced directions. The direction selectivity index (DSI) was calculated along the sampled orientation axis closest to the preferred direction according to the formula $DSI = (R_{pref} - R_{null})/(R_{pref} + R_{null})$, where R_{pref} is the response at the preferred direction and R_{null} is the response at the opposite direction.

The DSI of the response evoked by oscillatory drum movement was calculated as $DSI = (R_{TN} - R_{NT})/(R_{TN} + R_{NT})$, where R_{TN} is the response during the temporonasal phase of drum movement and R_{NT} is the response during the nasotemporal phase.

Onset latency and jitter

The onset latency of optogenetically evoked activity of NOT-DTN neurons was determined as the time lag between the beginning of the LED illumination and the time point at which the firing rate reached three times the standard deviation of spontaneous activity. Similarly, the onset latency of optogenetically evoked EPSCs in NOT-DTN neurons was determined as the time lag between the beginning of the LED illumination and the time point at which the EPSC amplitude reached three times the standard deviation of baseline noise. Trial-by-trial jitter of optogenetically evoked EPSCs was calculated as the standard deviation of the onset latency.

Overlap coefficient

Analysis of c-Fos immunohistochemistry was performed with ImageJ (National Institutes of Health). c-Fos-positive cells were identified as continuous pixels after thresholding and counted automatically. To quantify the extent of overlap between arborization of GFP-expressing RGC axons and c-Fos expression in the NOT-DTN, their boundaries were manually drawn and the overlap coefficient r was calculated as

$$r=\frac{\sum(S1_i \times S2_i)}{\sqrt{\sum (S1_i)^2 \times \sum (S2_i)^2}}$$

where $S1_i$ is 1 if pixel i is within the domain of RGC axons, otherwise 0; and $S2_i$ is 1 if pixel i is within the domain of c-Fos immunohistochemistry, otherwise 0 (Extended Data Fig. 5c).

Averaged normalized transfer function

For each animal, NOT-DTN multiunit activity was normalized to the average firing rate evoked by optimal spatial frequency. Data points of transfer functions from all animals were pooled, binned and averaged.

Vector analysis of the effect of cortical silencing on the transfer function

The vectors (arrows in Extended Data Fig. 9g–i) start at the centre of mass of data points obtained at a given spatial frequency under control conditions (grey) and end at the centre of mass of data points obtained at the same spatial frequency during cortical silencing trials (blue). The x-axis value of the centre of mass is the NOT-DTN multiunit firing rate averaged over trials obtained at a given spatial frequency, normalized by the average firing rate evoked by the best spatial frequency. The y-axis value of the centre of mass is the average OKR gain obtained during the same trials.

Inclusion/exclusion criteria

All samples or animals were included in the analysis except for the following exclusions: (1) in the analysis of OKR gain, trials in which video-oculography failed as a result of eye blinking or tears were excluded from analysis; (2) in Fig. 1g, h, one mouse was excluded from the analysis because its value of OKR potentiation was less than the threshold of 0.1; (3) in Fig. 3, two mice were excluded from the analysis because they were sick and lost a lot

in body weight during experiments; (4) in Figs. 4, 5, one mouse was excluded because the identification of NOT-DTN failed; and (5) in statistics of the activities of superior colliculus and vLGN, recordings which were identified *post hoc* as missing the target structures were excluded from the analysis. These criteria were pre-established.

Statistical analysis

Statistical analyses were done using statistics toolbox in Matlab. All data are presented as mean ± s.e.m. unless otherwise noted. Statistical significance was assessed using paired or unpaired *t*-tests and further confirmed with nonparametric Wilcoxon signed rank test or Wilcoxon rank sum test unless otherwise noted. Estimated sample sizes were retrospectively determined to achieve 80% power to detect expected effect sizes using Matlab. We did not intentionally select particular mice for treatment group or control group. No blinding was used. Owing to the limited sample size, the assumption of normal distribution was not tested. Nonparametric tests were used to confirm statistical significances reported by paired or unpaired *t*-tests. Thus, the conclusions of statistical tests were validated regardless of whether the data were normally distributed. The variance was not compared between groups. In *t*-tests, we assumed that samples were from distributions of unknown and unequal variances. The experiments were not randomized.

Extended Data

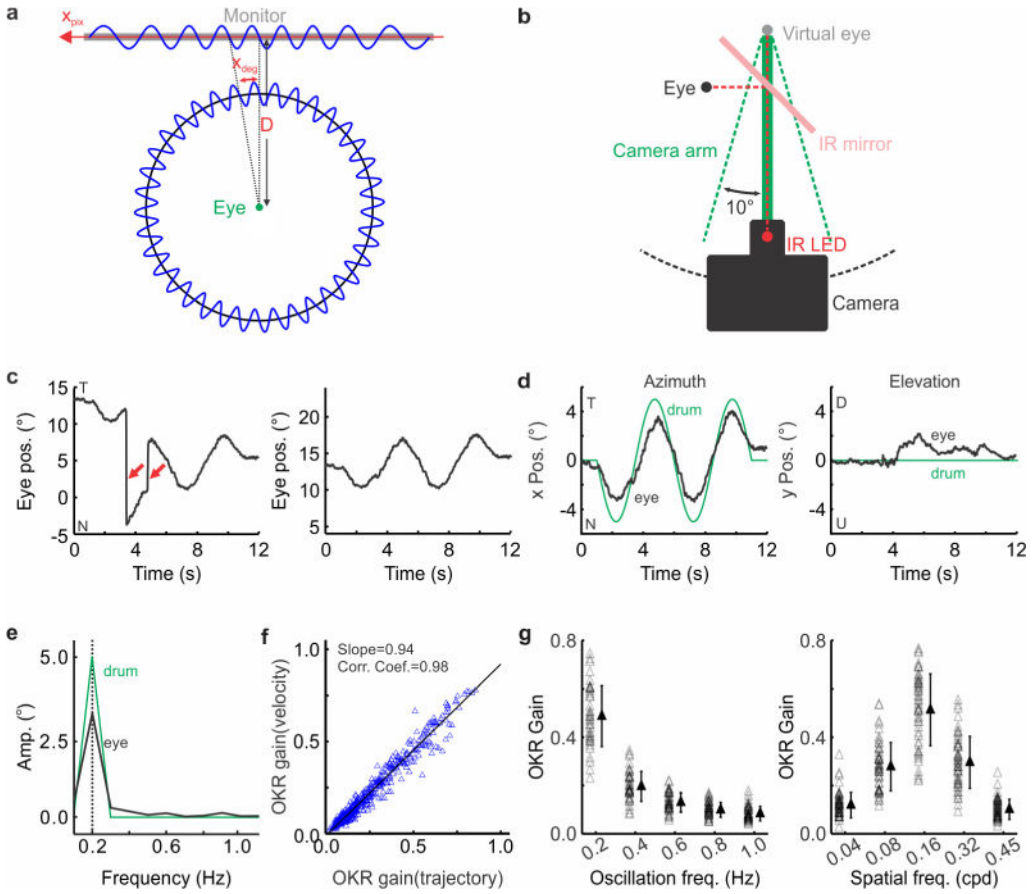

Extended Data Figure 1. Quantification of mouse OKR

a, Transformation of sinusoidal gratings from cylindrical coordinates of the virtual drum to Cartesian coordinates of the monitor. x_{pix} is the horizontal pixel position in Cartesian coordinates. D is the distance from the centre of monitors to the eye. x_{deg} is the azimuth angle of pixels in cylindrical coordinates. Note that the spatial period of the grating on the monitor is not uniform. See Methods for details. **b**, Schematic of calibration of the measurement of eye position. The camera is moved along a circumference centred on the image of the eye by ± 10°. **c–e**, Example traces of OKR eye trajectory and corresponding fast Fourier transform (FFT) spectra. **c**, Left, raw trace of one individual eye trajectory with both slow OKR component and fast saccade-like component (red arrows; T, temporal; N, nasal). Right, isolated OKR component after removal of the saccade-like component. Spatial frequency, 0.08 cpd; oscillation frequency, 0.2 Hz. **d**, Eye trajectories in horizontal azimuth (left) and vertical elevation (right) overlaid with corresponding drum trajectories (the same example as in **c**). Note that OKR eye movement is mainly restricted to the axis of the drum movement. D, down; U, up. **e**, Fourier transform spectra of eye trajectory and drum trajectory in **d** (left). The amplitude of the OKR trajectory peaks at the principal frequency (dotted line). **f**, OKR gain derived from OKR velocity versus OKR eye trajectory. Each point is one trial. Solid line, linear regression. **g**, Population summary of OKR gain evoked by five oscillation frequencies (left, spatial frequency 0.08 cpd) and five spatial frequencies (right, oscillation frequency 0.4 Hz). Each point is one mouse (n = 39 for oscillation frequency and 49 for spatial frequency). Data shown as mean ± s.d.

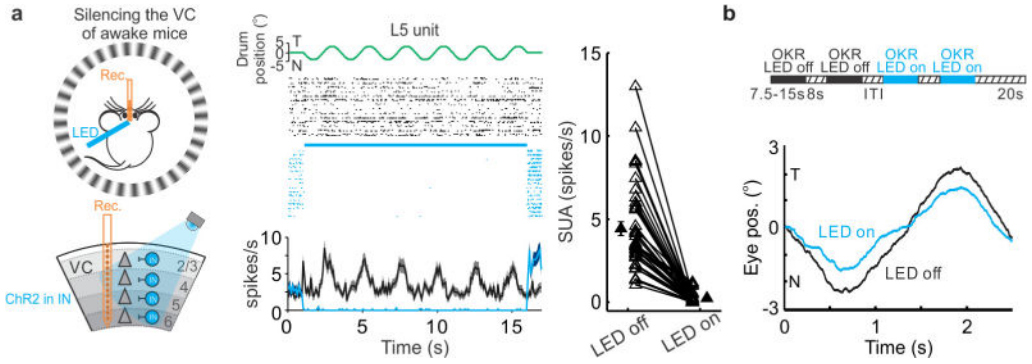

Extended Data Figure 2. Optogentic silencing of visual cortex

a, Left, schematic of experimental setup. IN, inhibitory neurons; VC, visual cortex. Middle, raster plot and PSTH of a single unit. Black, control condition; blue, cortical silencing. Blue bar, duration of blue light illumination (15 s). Control and photostimulation trials were interleaved (see **b**), but are separated here for clarity. Right, summary of firing rate of regular spiking units (n = 40). Data shown as mean ± s.e.m. **b**, Top, block design to examine the impact of cortical silencing on OKR performance. LED off, control trials; LED on, cortical silencing trials. Bottom, cycle averages of one individual OKR eye trajectory. T, temporal; N, nasal.

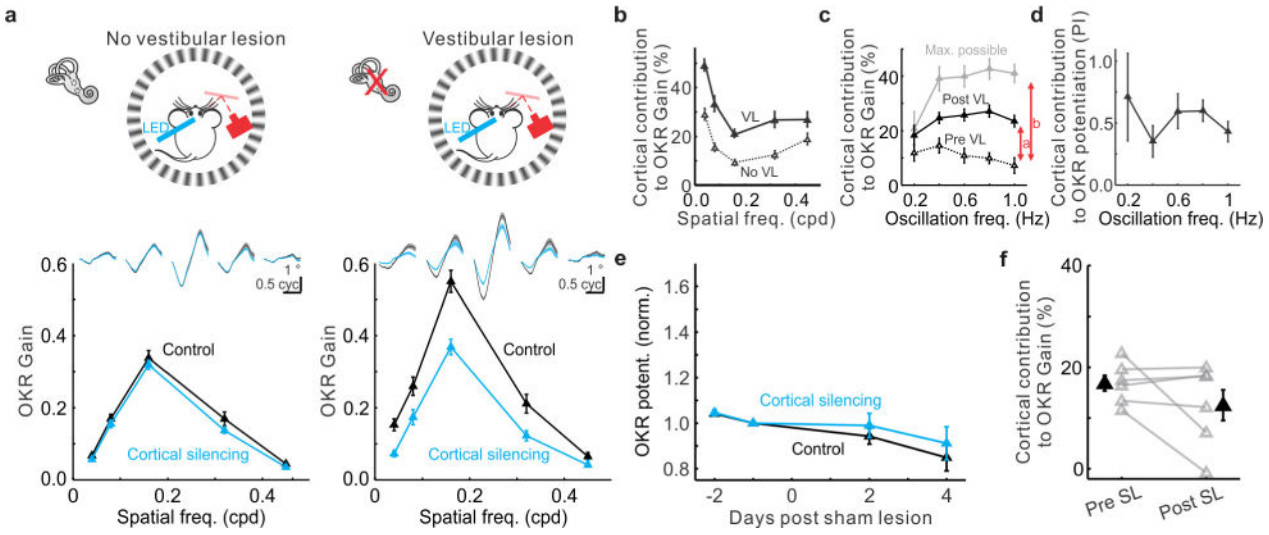

Extended Data Figure 3. Visual cortex contributes to OKR potentiation across spatial frequencies

a, Data from example mice. OKR performance of a naive animal (no vestibular lesion, left) and an animal with vestibular lesion (right). Top, schematic experimental setup. Bottom, cycle averages of all eye trajectories evoked by five spatial frequencies (oscillation frequency 0.4 Hz), and the corresponding OKR gains. Thickness of traces shows s.e.m. Data shown as mean ± s.e.m. **b**, Population average of cortical contribution to OKR gain at five spatial frequencies for animals with vestibular lesion (VL, solid line, $n = 17$ mice) and naive animals (no VL, dotted line, $n = 51$ mice). Data shown as mean ± s.e.m. **c**, Population average of cortical contribution to OKR gain at five oscillation frequencies before vestibular lesion (Pre VL, dotted line) and after vestibular lesion (Post VL, solid black line). The grey line is the maximal possible cortical contribution to OKR gain after vestibular lesion assuming the entire OKR potentiation depends on visual cortex (Max. possible) ($n = 13$ animals). Data shown as mean ± s.e.m. **d**, Population average of cortical contribution to OKR potentiation (potentiation index, PI) measured as the ratio between *a* and *b* (illustrated in **c**) at each oscillation frequency. Data shown as mean ± s.e.m. **e**, Population averages of pseudo-OKR potentiation following sham lesions. Black data points: no cortical silencing, normalized by OKR gain before sham lesions without cortical silencing. Blue data points: cortical silencing, normalized by OKR gain before sham lesions during cortical silencing ($n = 6$ mice). Data shown as mean ± s.e.m. **f**, Population summary of cortical contribution to OKR gain before (Pre SL) and after sham lesions (Post SL). Data shown as mean ± s.e.m.

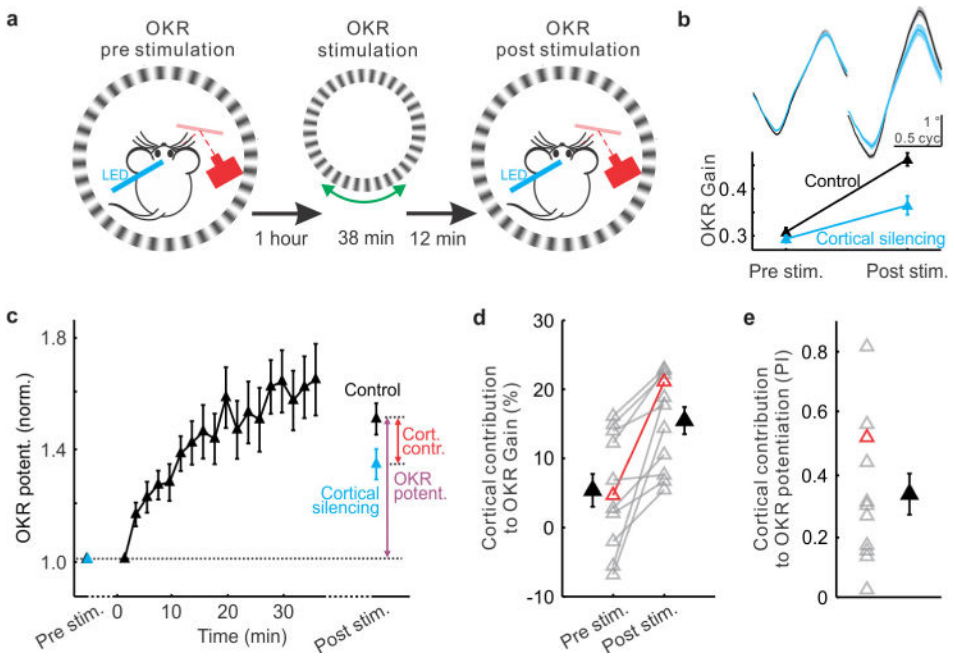

Extended Data Figure 4. Visual cortex contributes to OKR potentiation induced by continuous OKR stimulation

a, Schematic of experimental design. OKR gain before stimulation was measured twice, 1 day before and 1 h before continuous OKR stimulation (see Methods for details). **b**, Data from example mouse. Cycle averages of all eye trajectories and corresponding OKR gain before (Pre stim.) and after (Post stim.) continuous OKR stimulation (n = 576 cycles, spatial frequency 0.1 cpd, oscillation frequency 0.4 Hz). The thickness of the trace shows s.e.m. Note that following OKR stimulation cortical silencing leads to a larger reduction in OKR gain. Data shown as mean ± s.e.m. **c**, Population averaged time course of OKR potentiation induced by continuous OKR stimulation. Black, no cortical silencing (control), normalized by OKR gain before stimulation (Pre stim.) without cortical silencing. Blue, cortical silencing, normalized by OKR gain before stimulation during cortical silencing (n = 11 mice). Red arrow: the cortical contribution to OKR potentiation; magenta arrow: OKR potentiation. Data shown as mean ± s.e.m. **d**, Population summary of cortical contribution to OKR gain before (Pre stim.) and after stimulation (Post stim.) (n =11 mice). Red data points: the animal in **b**. Data shown as mean ± s.e.m. **e**, Population summary of cortical contribution to OKR potentiation (potentiation index, PI) (n = 11 mice). Red data point: the animal in **b**. Data shown as mean ± s.e.m.

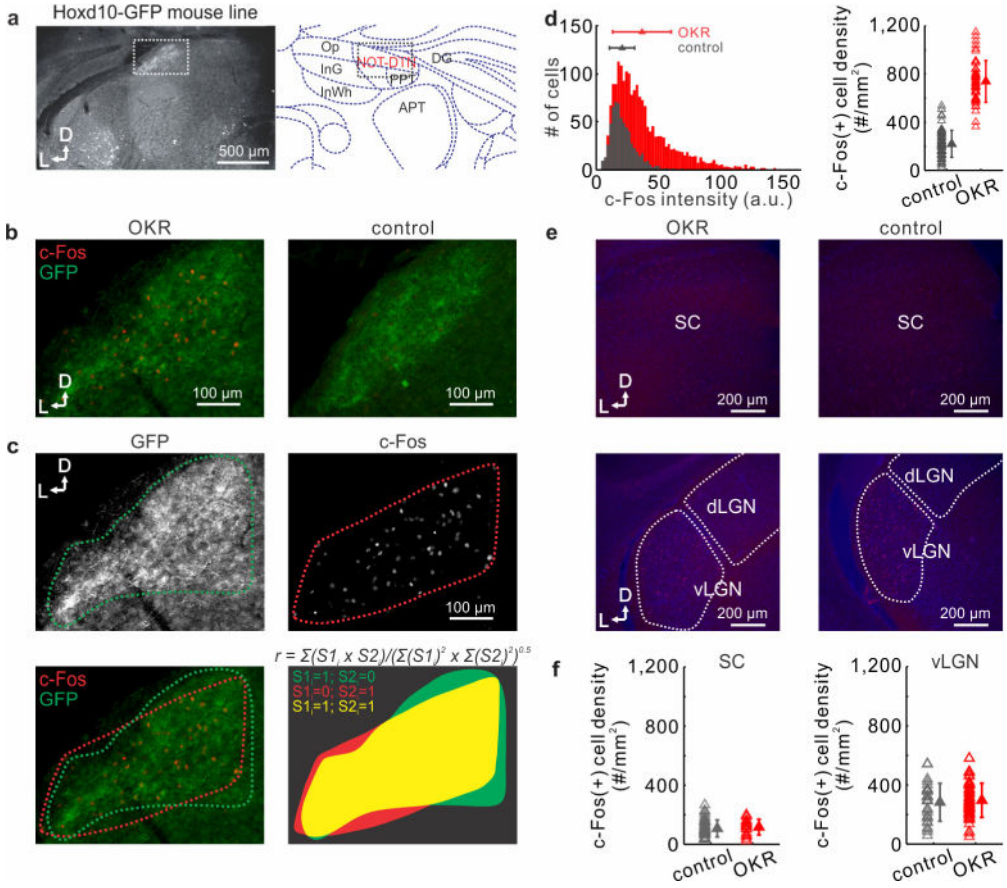

Extended Data Figure 5. Identification of the NOT-DTN based on retinal input and c-Fos expression

a, Left, coronal section of NOT-DTN of Hoxd10-GFP mouse. The distribution of GFP-expressing RGC axons delineates the NOT-DTN (dotted box). Right, delineation of NOT-DTN and surrounding nuclei (modified from Paxinos, G. & Franklin, K. *The Mouse Brain in Stereotaxic Coordinates* (Elsevier, 2007)) for the corresponding coronal plane. D, dorsal; L, lateral. **b**, **c**-Fos immunostaining of coronal slices containing NOT-DTN of Hoxd10-GFP mice. Left, section from an animal that underwent OKR stimulation. Note that the distribution of GFP RGC axons overlaps with that of c-Fos-positive cells. Right, section from an animal that did not undergo OKR stimulation (control). **c**, Quantification of the extent of overlap between GFP RGC axons and c-Fos-positive cells in **b** (left). Top left, boundary of the domain of RGC axons. Top right, boundary of the domain of c-Fos-positive cells. Bottom left, overlay of those two boundaries. Bottom right, calculation of overlap coefficient r of those two domains (see Methods). **d**, Left, histogram of fluorescence intensity of c-Fos-positive cells. Data shown as mean ± s.d. $P < 10^{-20}$. Right, summary of density of c-Fos-positive cells in NOT-DTN. Each data point represents one slice. Data shown as mean ± s.d. $P < 10^{-20}$. $n = 50$ slices from 4 mice of OKR group and 59 slices from 4 mice of control group. **e**, c-Fos immunostaining of coronal slices containing superior colliculus (SC, top) or vLGN (bottom). Blue, DAPI; red, c-Fos. **f**, Summary of density of c-Fos-positive cells in superior colliculus (left) and vLGN (right). Each data point represents one slice. Data shown as mean ± s.d. $n = 4$ mice for both OKR group and control group.

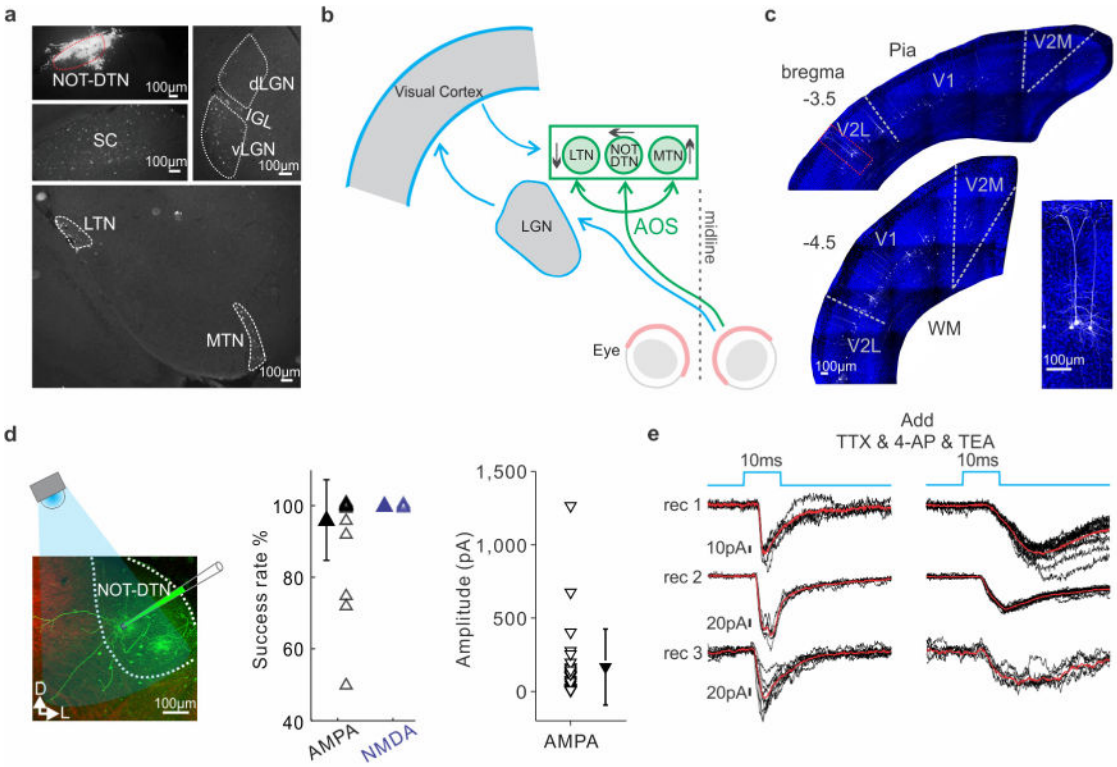

Extended Data Figure 6. Structures projecting to NOT-DTN and monosynaptic transmission between visual cortex and NOT-DTN

a, Subcortical structures labelled by retro-beads injected into the NOT-DTN. Top left, injection site. SC, superior colliculus; dLGN, dorsal lateral geniculate nucleus; IGL, intergeniculate leaflet; vLGN, ventral lateral geniculate nucleus; LTN, lateral terminal nucleus; MTN, medial terminal nucleus. **b**, Schematic drawing of the two pathways relaying visual information to the AOS. Thalamo-cortical-NOT-DTN pathway is outlined in blue, retinal pathway outlined in green. **c**, Spatial distribution of NOT-DTN-projecting neurons in visual cortex (visual cortex injected with Flex-tdTomato and NOT-DTN with Cav2-Cre) for two coronal sections. Boundaries between primary and secondary areas are drawn according to Paxinos, G. & Franklin, K. *The Mouse Brain in Stereotaxic Coordinates* (Elsevier, 2007). Inset on the right, higher magnification of the region shown in the red box. Blue, DAPI; white, tdTomato. **d**, Left, schematic of the setup for *in vitro* whole-cell voltage-clamp recording from NOT-DTN neurons in acute slices. Green, patched NOT-DTN neurons; red, axons from visual cortex. D, dorsal; L, lateral. Middle, summary of success rate of EPSCs evoked by optogenetic stimulation of cortico-fugal axons. Right, peak amplitude of AMPA receptor mediated EPSCs. Data shown as mean ± s.d. Each data point represents one NOT-DTN recording. **e**, Left, AMPA receptor-mediated EPSCs evoked by optogenetic stimulation of cortico-fugal axons for three NOT-DTN neurons voltage-clamped at −65 mV Right, AMPA receptor-mediated EPSCs of the same cells after blocking multi-synaptic components with TTX (sCRACM). Black, individual trials; red, average; blue, time course of blue light illumination.

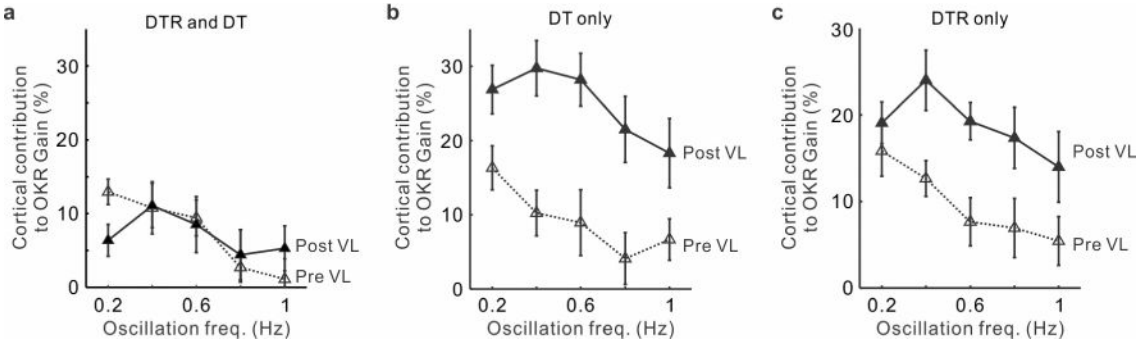

Extended Data Figure 7. Cortical contribution to OKR gain at different oscillation frequencies in animals with spared or ablated cortical projection to the NOT-DTN

a, Population averages of cortical contribution to OKR gain at five different oscillation frequencies before (dotted line, Pre VL) and after (solid line, Post VL) vestibular lesion for mice in which the cortico-fugal projection was ablated (n = 18 animals). Data shown as mean ± s.e.m. **b**, **c**, Population averages of cortical contribution to OKR gain at five different oscillation frequencies for mice in which the infection with diphtheria toxin receptor (DTR) (**b**) or injection of diphtheria toxin (DT) (**c**) was omitted (n = 8 and 6 animals, respectively). Data shown as mean ± s.e.m.

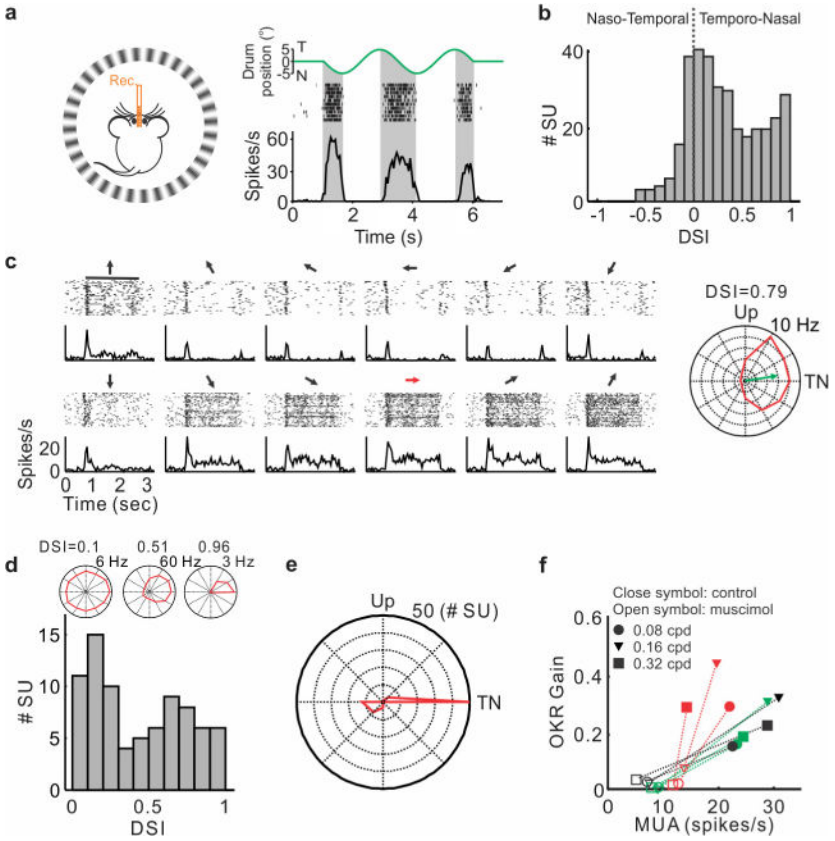

Extended Data Figure 8. Tuning properties of NOT-DTN neurons

a, Left, schematic of experimental setup; mouse under anaesthesia. Right, raster plot and PSTH of an example single unit. Shades indicate the temporonasal phase of drum trajectory.

b, Histogram of direction selectivity index (DSI) of single units in NOT-DTN stimulated by oscillatory drum movement. **c**, Example single unit. Left, raster plot and PSTH of responses evoked by moving gratings of 12 equally spaced directions (indicated by arrows, red arrow for temporonasal direction). Bar, duration of stimulation. Right, polar plot of the same unit. Green arrow, preferred direction. **d**, Top, example polar plots of weak DSI, medium DSI and strong DSI units. Bottom, histogram of DSI of NOT-DTN units stimulated by grating movement of 12 directions. **e**, Summary of preferred direction for NOT-DTN units with DSI greater than 0.1. Note the dominant preference for temporonasal direction. **f**, OKR gain and NOT-DTN multi-unit activity recorded before (closed) and after (open) silencing NOT-DTN with muscimol. Each colour represents one animal. Note that strong suppression of NOT-DTN activity leads to the abolishment of the OKR. Mice were awake during recording.

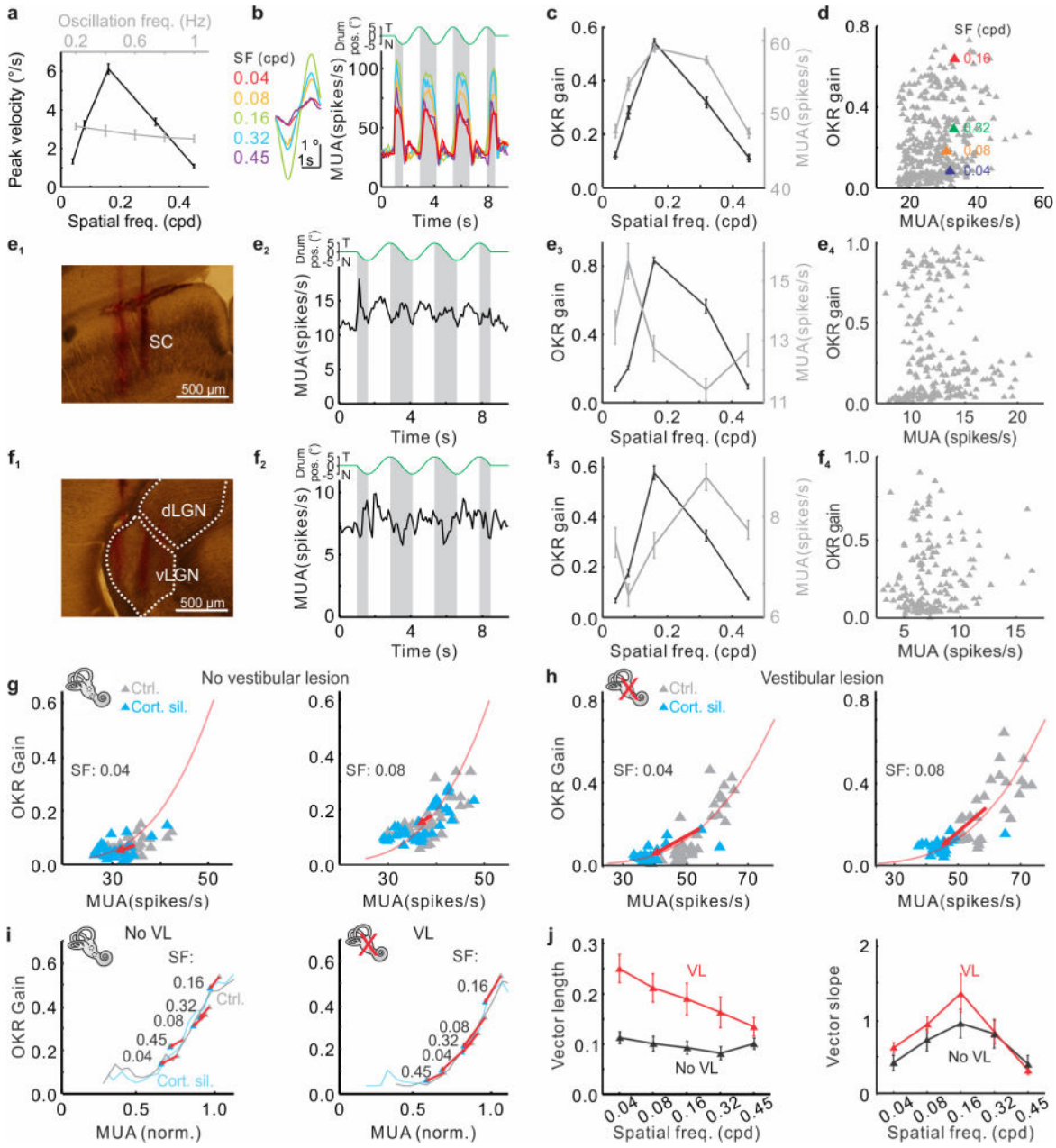

Extended Data Figure 9. Cortical silencing induces a larger shift along the transfer function after vestibular lesion

a, Example spatial frequency tuning and oscillation frequency tuning curves of OKR peak velocity. Note that while the OKR peak velocity is modulated by the spatial frequency of the drum stimulus (black), it is constant across oscillation frequencies (grey). Data shown as mean ± s.e.m. **b**, Data from example mouse. Left, cycle averages of all eye trajectories triggered by five different spatial frequencies. Right, the corresponding PSTH of NOT-DTN multi-unit activity. Note the correlation between the amplitude of eye trajectory and the amplitude of activity. Shades indicate the temporonasal phase of drum trajectory. **c**, Spatial frequency tuning curves of OKR gain (black) and NOT-DTN activity (grey) from **b**. Data shown as mean ± s.e.m. **d**, Pseudotransfer function from the animal shown in Fig. 5b using

the firing rate during the nasotemporal instead of the temporonasal phase. Each data point represents one trial. Coloured triangles represent the same trials as illustrated in Fig. 5b (middle). Note the lack of correlation between OKR gain and the nasotemporal phase of multi-unit activity (MUA) recorded in NOT-DTN. **e**, Example spiking activity in superior colliculus (SC) during OKR stimulation. **e$_1$**, Image of coronal slice containing superior colliculus. Red, electrode track labelled with DiI. **e$_2$**, PSTH of superior colliculus MUA. **e$_3$**, Spatial frequency tuning curves of OKR gain (black) and superior colliculus activity (grey). Data shown as mean ± s.e.m. **e$_4$**, Pseudo-transfer function using superior colliculus activity. Note the lack of correlation between OKR gain and MUA recorded in superior colliculus. **f**, As in **e**, except for spiking activity in ventral lateral geniculate nucleus (vLGN) during OKR stimulation. Note the lack of correlation between OKR gain and MUA recorded in vLGN. Data shown as mean ± s.e.m. **g**, Data from example mouse. Recording from NOT-DTN. Shift along the transfer function upon cortical silencing for data points obtained at two different spatial frequencies (SF; left, 0.04 cpd; right, 0.08 cpd) in a naive animal (no vestibular lesion). The vector (arrow) connects the centres of mass of control (grey) and cortical silencing trials (blue) obtained at the same spatial frequency. Red line, transfer function computed with data obtained at all tested spatial frequencies under control conditions (that is, without cortical silencing). **h**, As in **g**, except for an animal with vestibular lesion. Note longer vectors as compared to **g**. **i**, Population summary of vectors for five different spatial frequencies computed on averaged normalized transfer functions in naive animals (no VL; left; $n = 17$) and animals with vestibular lesion (VL; right; $n = 17$). **j**, Population averages of vector lengths (left) and slopes (right) for naive animals (no VL; black; $n = 17$) and animals with vestibular lesion (VL; red; $n = 17$). Data shown as mean ± s.e.m.

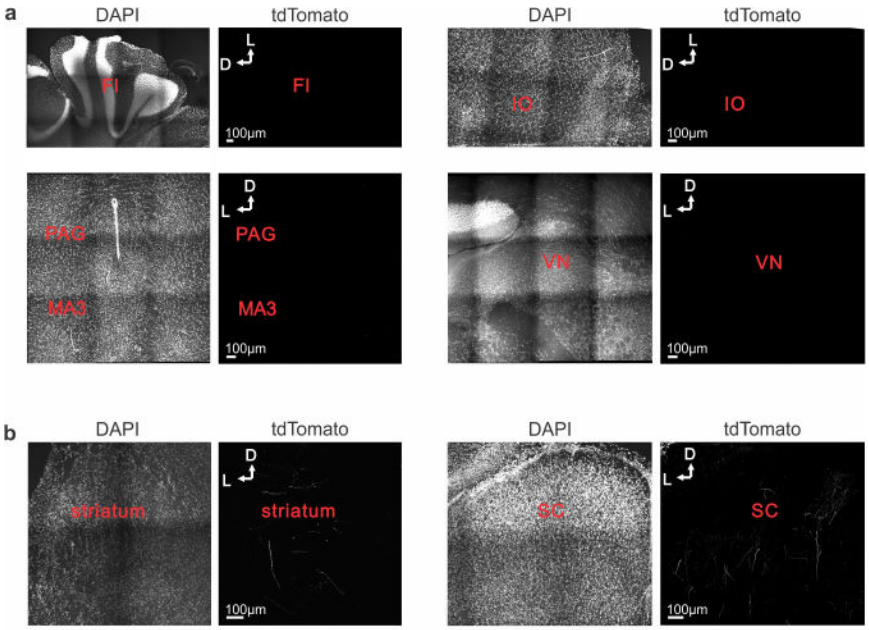

Extended Data Figure 10. Presence and absence of collaterals from NOT-DTN-projecting cortical neurons in selected brain areas

a, Absence of collaterals from NOT-DTN-projecting cortical neurons in flocculus (FL); inferior olive (IO); periaqueductal grey (PAG); medial accessory oculomotor nucleus (MA3); and vestibular nuclei (VN). For each coronal section the left panel is the DAPI fluorescence signal (blue channel) and the right panel is the tdTomato fluorescence signal (red channel). **b**, Presence of collaterals from NOT-DTN-projecting cortical neurons in the striatum and superior colliculus (SC).

Acknowledgments

We thank members of the Scanziani and Isaacson laboratories for advice on this project; J. Evora, N. Kim, M. Chan and A. Linder for technical support; T. M. Jessell for sharing the Flex.DTR.GFP plasmid and virus; M. Faulstich and S. du Lac for sharing eye tracking codes and advice on vestibular lesions; D. Li for advice on statistical analysis; J. Isaacson for comments on the manuscript; S. R. Olsen for sharing codes for *in vivo* recordings and unit isolation; and M. Xue for help with *in vitro* recordings. M.S. is an investigator of the Howard Hughes Medical Institute. This work was supported by the Gatsby Charitable Foundation and the US National Institutes of Health (R01 EY025668).

References

1. Sherman, SM., Guillery, RW. Functional Connections of Cortical Areas: A New View from the Thalamus. MIT Press; 2013.
2. Guillery RW. Anatomical pathways that link perception and action. Prog Brain Res. 2005; 149:235–256. [PubMed: 16226588]
3. Giolli RA, Blanks RH, Lui F. The accessory optic system: basic organization with an update on connectivity, neurochemistry, and function. Prog Brain Res. 2006; 151:407–440. [PubMed: 16221596]
4. Kawai R, et al. Motor cortex is required for learning but not for executing a motor skill. Neuron. 2015; 86:800–812. [PubMed: 25892304]
5. Distler, C., Hoffmann, KP. The Oxford Handbook of Eye Movements. Oxford Univ. Press; 2011. p. 65-83.
6. Simpson JI. The accessory optic system. Annu Rev Neurosci. 1984; 7:13–41. [PubMed: 6370078]
7. Faulstich BM, Onori KA, du Lac S. Comparison of plasticity and development of mouse optokinetic and vestibulo-ocular reflexes suggests differential gain control mechanisms. Vision Res. 2004; 44:3419–3427. [PubMed: 15536010]
8. Lisberger SG, Miles FA, Optican LM, Eighmy BB. Optokinetic response in monkey: underlying mechanisms and their sensitivity to long-term adaptive changes in vestibuloocular reflex. J Neurophysiol. 1981; 45:869–890. [PubMed: 7241174]
9. Prusky GT, Silver BD, Tschetter WW, Alam NM, Douglas RM. Experience-dependent plasticity from eye opening enables lasting, visual cortex-dependent enhancement of motion vision. J Neurosci. 2008; 28:9817–9827. [PubMed: 18815266]
10. Katoh A, Kitazawa H, Itohara S, Nagao S. Dynamic characteristics and adaptability of mouse vestibulo-ocular and optokinetic response eye movements and the role of the flocculo-olivary system revealed by chemical lesions. Proc Natl Acad Sci USA. 1998; 95:7705–7710. [PubMed: 9636214]
11. Faulstich M, van Alphen AM, Luo C, du Lac S, De Zeeuw CI. Oculomotor plasticity during vestibular compensation does not depend on cerebellar LTD. J Neurophysiol. 2006; 96:1187–1195. [PubMed: 16723418]
12. Gittis AH, du Lac S. Intrinsic and synaptic plasticity in the vestibular system. Curr Opin Neurobiol. 2006; 16:385–390. [PubMed: 16842990]
13. Kawato M, Gomi H. The cerebellum and VOR/OKR learning models. Trends Neurosci. 1992; 15:445–453. [PubMed: 1281352]
14. Fetter M, Zee DS, Proctor LR. Effect of lack of vision and of occipital lobectomy upon recovery from unilateral labyrinthectomy in rhesus monkey. J Neurophysiol. 1988; 59:394–407. [PubMed: 3258363]

15. Tusa RJ, Demer JL, Herdman SJ. Cortical areas involved in OKN and VOR in cats: cortical lesions. J Neurosci. 1989; 9:1163–1178. [PubMed: 2703872]
16. Fetter M, Zee DS. Recovery from unilateral labyrinthectomy in rhesus monkey. J Neurophysiol. 1988; 59:370–393. [PubMed: 3258362]
17. Paige GD. Plasticity in the vestibulo-ocular and optokinetic reflexes following modification of canal input. Rev Oculomot Res. 1985; 1:145–153. [PubMed: 3940026]
18. McCall AA, Yates BJ. Compensation following bilateral vestibular damage. Front Neurol. 2011; 2:88. [PubMed: 22207864]
19. Reid RC, Alonso JM. The processing and encoding of information in the visual cortex. Curr Opin Neurobiol. 1996; 6:475–480. [PubMed: 8794104]
20. Tabata H, Shimizu N, Wada Y, Miura K, Kawano K. Initiation of the optokinetic response (OKR) in mice. J Vision. 2010; 10:11–17.
21. Distler C, Hoffmann KP. Cortical input to the nucleus of the optic tract and dorsal terminal nucleus (NOT-DTN) in macaques: a retrograde tracing study. Cereb Cortex. 2001; 11:572–580. [PubMed: 11375918]
22. Berson DM, Graybiel AM. Some cortical and subcortical fiber projections to the accessory optic nuclei in the cat. Neuroscience. 1980; 5:2203–2217. [PubMed: 7465052]
23. Hoffmann KP, Distler C. Quantitative analysis of visual receptive fields of neurons in nucleus of the optic tract and dorsal terminal nucleus of the accessory optic tract in macaque monkey. J Neurophysiol. 1989; 62:416–428. [PubMed: 2769338]
24. Grasse KL, Cynader MS. Electrophysiology of lateral and dorsal terminal nuclei of the cat accessory optic system. J Neurophysiol. 1984; 51:276–293. [PubMed: 6707722]
25. Collewijn H. Oculomotor areas in the rabbits midbrain and pretectum. J Neurobiol. 1975; 6:3–22. [PubMed: 1185174]
26. Distler C, Mustari MJ, Hoffmann KP. Cortical projections to the nucleus of the optic tract and dorsal terminal nucleus and to the dorsolateral pontine nucleus in macaques: a dual retrograde tracing study. J Comp Neurol. 2002; 444:144–158. [PubMed: 11835187]
27. Baldauf ZB, Wang XP, Wang S, Bickford ME. Pretectotectal pathway: an ultrastructural quantitative analysis in cats. J Comp Neurol. 2003; 464:141–158. [PubMed: 12898608]
28. Xiong XR, et al. Auditory cortex controls sound-driven innate defense behaviour through corticofugal projections to inferior colliculus. Nat Commun. 2015; 6:7224. [PubMed: 26068082]
29. Liang F, et al. Sensory cortical control of a visually induced arrest behavior via corticotectal projections. Neuron. 2015; 86:755–767. [PubMed: 25913860]
30. Bajo VM, Nodal FR, Moore DR, King AJ. The descending corticocollicular pathway mediates learning-induced auditory plasticity. Nat Neurosci. 2010; 13:253–260. [PubMed: 20037578]
31. Zhao S, et al. Cell type-specific channelrhodopsin-2 transgenic mice for optogenetlc dissection of neural circuitry function. Nat Methods. 2011; 8:745–752. [PubMed: 21985008]
32. Hippenmeyer S, et al. A developmental switch in the response of DRG neurons to ETS transcription factor signaling. PLoS Biol. 2005; 3:e159. [PubMed: 15836427]
33. Taniguchi H, et al. A resource of Cre driver lines for genetic targeting of GABAergic neurons in cerebral cortex. Neuron. 2011; 71:995–1013. [PubMed: 21943598]
34. Dhande OS, et al. Genetic dissection of retinal inputs to brainstem nuclei controlling image stabilization. J Neurosci. 2013; 33:17797–17813. [PubMed: 24198370]
35. Nagel G, et al. Channelrhodopsin-2, a directly light-gated cation-selective membrane channel. Proc Natl Acad Sci USA. 2003; 100:13940–13945. [PubMed: 14615590]
36. Boyden ES, Zhang F, Bamberg E, Nagel G, Deisseroth K. Millisecond-timescale, genetically targeted optical control of neural activity. Nat Neurosci. 2005; 8:1263–1268. [PubMed: 16116447]
37. Azim E, Jiang J, Alstermark B, Jessell TM. Skilled reaching relies on a V2a propriospinal internal copy circuit. Nature. 2014; 508:357–363. [PubMed: 24487617]
38. Soudais C, Laplace-Builhe C, Kissa K, Kremer EJ. Preferential transduction of neurons by canine adenovirus vectors and their efficient retrograde transport in vivo. FASEB J. 2001; 15:2283–2285. [PubMed: 11511531]

39. Prusky GT, Alam NM, Beekman S, Douglas RM. Rapid quantification of adult and developing mouse spatial vision using a virtual optomotor system. Invest Ophthalmol Vis Sci. 2004; 45:4611–4616. [PubMed: 15557474]

40. Collewijn H. Optokinetic eye movements in the rabbit: input-output relations. Vision Res. 1969; 9:117–132. [PubMed: 5778032]

41. Stahl JS, van Alphen AM, De Zeeuw CI. A comparison of video and magnetic search coil recordings of mouse eye movements. J Neurosci Methods. 2000; 99:101–110. [PubMed: 10936649]

42. Stahl JS. Calcium channelopathy mutants and their role in ocular motor research. Ann NY Acad Sci. 2002; 956:64–74. [PubMed: 11960794]

43. Olsen SR, Bortone DS, Adesnik H, Scanziani M. Gain control by layer six in cortical circuits of vision. Nature. 2012; 483:47–52. [PubMed: 22367547]

44. Liu BH, et al. Intervening inhibition underlies simple-cell receptive field structure in visual cortex. Nat Neurosci. 2010; 13:89–96. [PubMed: 19946318]

45. Petreanu L, Mao T, Sternson SM, Svoboda K. The subcellular organization of neocortical excitatory connections. Nature. 2009; 457:1142–1145. [PubMed: 19151697]

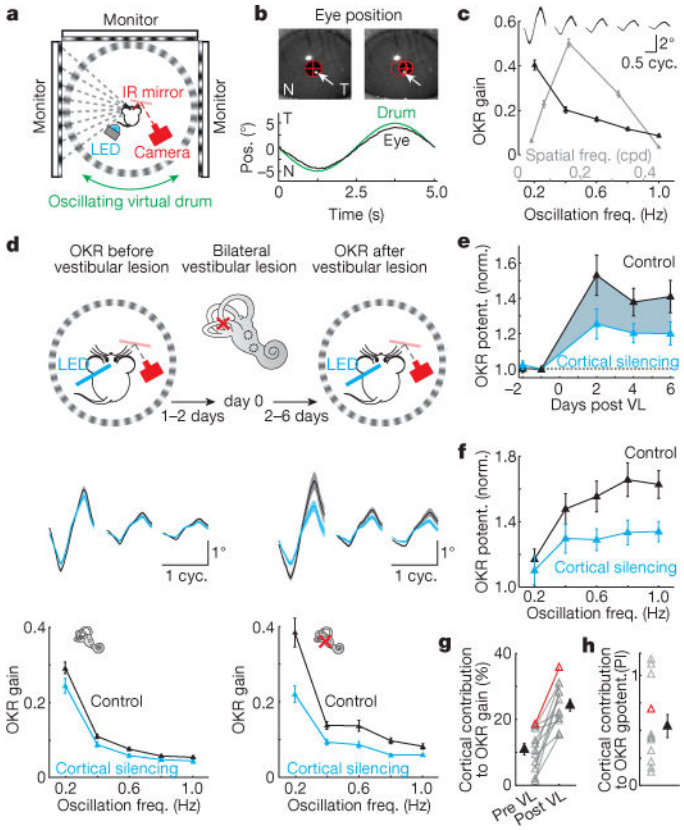

Figure 1. Visual cortex contributes to OKR potentiation

a, Schematic of experimental setup. **b**, Top, snapshots of nasal (N; left) and temporal (T; right) eye positions. Red ellipses, pupil fit. Red crosses, pupil centres. Arrows, corneal reflection of reference LED. Bottom, cycle average of individual eye trajectory overlaid with drum trajectory. **c**, Data from example mouse. Oscillation frequency and spatial frequency tuning curves (n = 32 and 48 trials, respectively). Top traces, cycle-averaged OKR trajectories (n = 96–720 cycles). Thickness, s.e.m. **d**, Data from example mouse. Top, schematic of experimental design. Bottom, oscillation frequency tuning curves of OKR gain before vestibular lesion (VL; left, n = 60 trials) and 2 days after vestibular lesion (right, n = 30 trials). Blue and black curves, with and without cortical silencing. Top traces, cycle-averaged OKR trajectories (n = 120–600 cycles). Thickness, s.e.m. **e**, Population average of OKR potentiation following vestibular lesion. Black, no cortical silencing. Blue, cortical silencing (n = 13 mice). Shaded area illustrates cortical contribution to OKR potentiation. **f**, Population tuning curves of OKR potentiation following vestibular lesion (n = 13 mice). **g**, Population summary of cortical contribution to OKR gain before (Pre VL) and after vestibular lesion (Post VL). **h**, Population summary of cortical contribution to OKR potentiation (potentiation index, PI). Red data point in **g** and **h**: animal in **d**. n = 12 mice for **g** and **h**. Data in **c**–**h** shown as mean ± s.e.m.

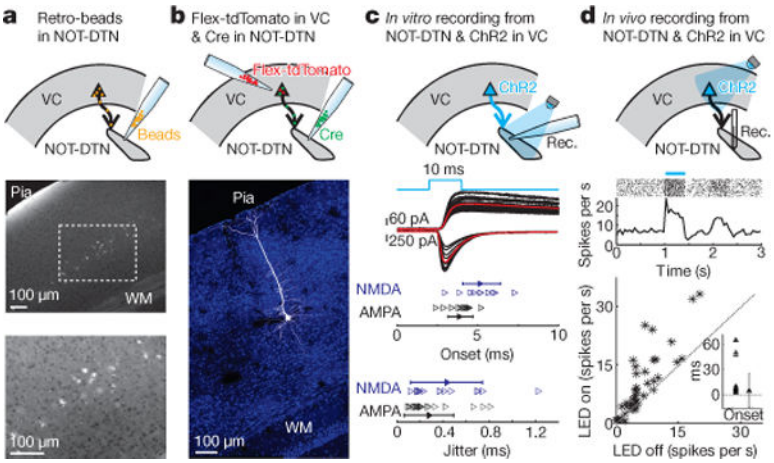

Figure 2. Cortico-fugal projection from mouse visual cortex to NOT-DTN

a–d, Top, schematic of experimental design. VC, visual cortex. **a**, Beads injected into NOT-DTN are retrogradely transported to visual cortex. Middle, coronal slice of visual cortex. Bottom, higher magnification of the enclosed area. WM, white matter. **b**, Example of layer 5 pyramidal cell projecting to NOT-DTN in visual cortex. Blue, DAPI; white, tdTomato. **c**, Middle, AMPA receptor-mediated (downwards) or NMDA receptor-mediated (upwards) EPSCs evoked in NOT-DTN neurons by optogenetic stimulation of cortico-fugal axons *in vitro*. Black, individual traces; red, average traces; blue, time course of blue light illumination. Bottom, summary of onset latency and trial-by-trial jitter of EPSCs. Data shown as mean ± s.d.; $n = 9$ mice. **d**, Firing of NOT-DTN neurons upon optogenetic activation of visual cortex *in vivo*. Middle, raster plot and PSTH of a NOT-DTN unit. Blue bar, LED illumination. Bottom, firing rates of NOT-DTN units in LED-off trials vs LED-on trials. Dotted line, unity line. Inset, summary of onset latency ($n = 23$ units). Data shown as median ± s.d.; $n = 4$ mice.

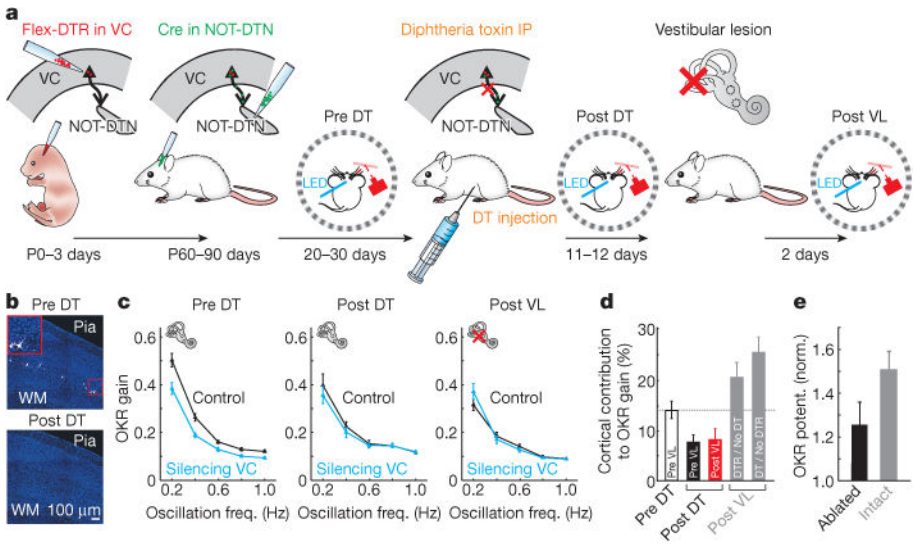

Figure 3. Cortico-fugal projection to NOT-DTN is necessary for OKR potentiation

a, Schematic of experimental design. DTR, diphtheria toxin receptor; DT, diphtheria toxin; VL, vestibular lesion. **b**, Coronal slices of visual cortex from a mouse without diphtheria toxin injection (top) or with diphtheria toxin injection (bottom). Inset, higher magnification of the enclosed area. Blue, DAPI; white, GFP. **c**, Data from example mouse. Oscillation frequency tuning curves measured before ablation of the cortico-fugal projections (Pre DT, n = 60 trials), after ablation (Post DT, n = 30 trials) and after vestibular lesion (Post VL, n = 42 trials). **d**, Population average of cortical contribution to OKR gain. White, intact cortico-fugal projection. Black, after ablation of the cortico-fugal projection and before vestibular lesion. Red, after vestibular lesion. Same set of animals (n = 18 mice). Grey columns, two control groups after vestibular lesion: left, without diphtheria toxin injection (n = 6 mice); right, without DTR infection (n = 8 mice). **e**, Population average of OKR potentiation for mice with intact or ablated cortico-fugal projections (n = 27 and 18 mice, respectively). Data in **c–e** shown as mean ± s.e.m.

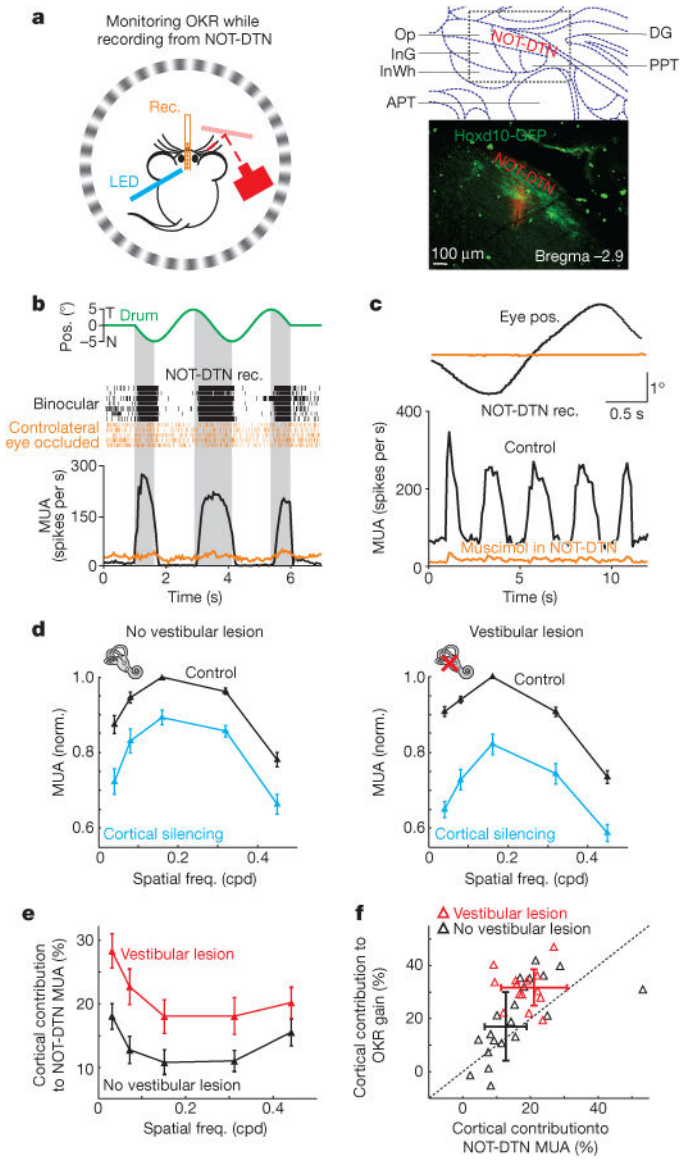

Figure 4. Enhanced cortical modulation of NOT-DTN activity with OKR potentiation

a, Left, schematic of experimental setup. Right, top, NOT-DTN and surrounding nuclei (modified from Paxinos, G. & Franklin, K. *The Mouse Brain in Stereotaxic Coordinates* (Elsevier, 2007)); bottom, coronal slice of NOT-DTN from Hoxd10-GFP mouse. Green, GFP; red, electrode track labelled with DiI. **b**, Data from example mouse. Top, drum trajectory. Shaded areas, temporo-nasal phase of drum trajectory. Bottom, raster plot and post-stimulus time histogram (PSTH) of NOT-DTN multiunit activity (n = 30 and 18 trials for binocular (black) and ipsilateral vision (orange), respectively). **c**, Data from example mouse. Cycle averages of all eye trajectories (top) and simultaneously recorded NOT-DTN activity (bottom) before (black; n = 49 trials) and after silencing NOT-DTN with muscimol (orange; n = 49 trials). **d**, Population tuning curves of NOT-DTN activity for naive mice (no vestibular lesion, n = 17 mice) and mice with vestibular lesion (n = 17 mice). Curves normalized to best frequency in control. Data shown as mean ± s.e.m. **e**, Population tuning

curves of cortical contribution to NOT-DTN activity (n = 17 mice for both groups). Data shown as mean ± s.e.m. **f**, Correlation between cortical contribution to OKR gain and cortical contribution to NOT-DTN activity in naive animals (black, no vestibular lesion) and lesioned animals (red; correlation coefficient, 0.55). Data shown as mean ± s.d.; dotted line, unity line.

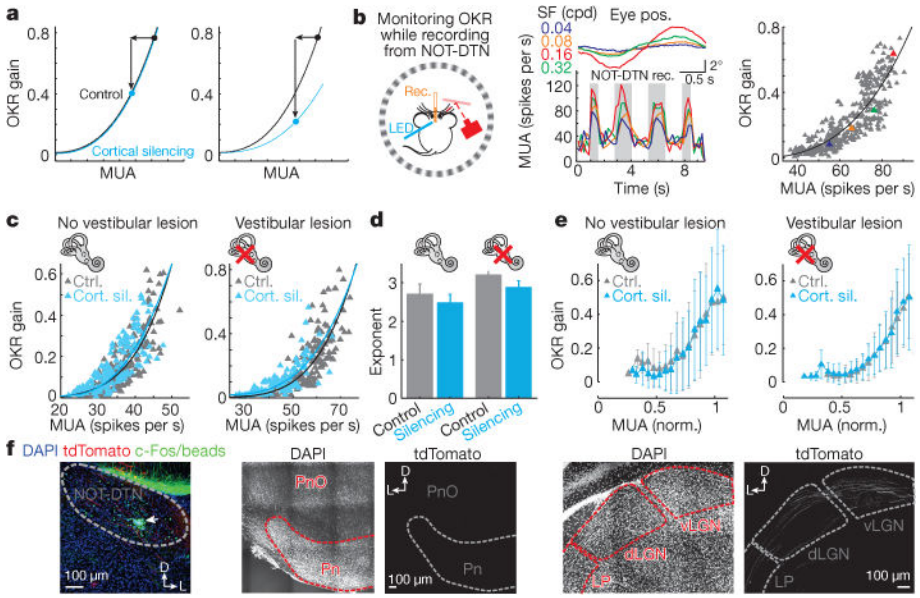

Figure 5. Impact of cortex on NOT-DTN activity matches cortical contribution to OKR potentiation

a, Model transfer functions. Left, reduction in NOT-DTN activity (leftward arrow) upon cortical silencing leads to a reduction in OKR gain (downward arrow) predicted by the transfer function obtained under control conditions. Right, reduction in OKR gain upon cortical silencing is larger than predicted by the transfer function. **b**, Data from example mouse. Left, schematic of experimental setup. Middle, cycle averages of OKR trajectory (top, $n = 3$ cycles) and PSTH of simultaneously recorded NOT-DTN activity (bottom) in individual trials of four different spatial frequencies (colour coded). Right, transfer function. Each data point is one trial. Coloured triangles, trials illustrated in the middle. MUA, firing rate during the temporo-nasal phase (shaded in PSTH). Solid curve, best fit of power function. **c**, Data from example mice. Transfer functions of a naive mouse (no vestibular lesion) and a mouse with vestibular lesion. **d**, Population averages of exponent of transfer functions for naive (non-lesioned, $n = 17$) and lesioned mice ($n = 17$). **e**, Population-averaged normalized transfer functions for naive (non-lesioned) and lesioned mice. Data shown as mean ± s.d. **f**, Left, confocal image of NOT-DTN. White arrow, injection site of CAV2-Cre virus. Middle and right, confocal images of pontine nuclei (Pn) and visual thalamus (LP, dLGN and vLGN). D, dorsal; L, lateral.